

# A Second-Order Unsplit Godunov Scheme for Cell-Centered MHD: the CTU-GLM scheme.

Andrea Mignone<sup>\*,a</sup>, Petros Tzeferacos<sup>a</sup>

<sup>a</sup>*Dipartimento di Fisica Generale, Università degli studi di Torino*

---

## Abstract

We assess the validity of a single step Godunov scheme for the solution of the magneto-hydrodynamics equations in more than one dimension. The scheme is second-order accurate and the temporal discretization is based on the dimensionally unsplit Corner Transport Upwind (CTU) method of Colella. The proposed scheme employs a cell-centered representation of the primary fluid variables (including magnetic field) and conserves mass, momentum, magnetic induction and energy. A variant of the scheme, which breaks momentum and energy conservation, is also considered. Divergence errors are transported out of the domain and damped using the mixed hyperbolic/parabolic divergence cleaning technique by Dedner et al. (J. Comput. Phys., 175, 2002). The strength and accuracy of the scheme are verified by a direct comparison with the eight-wave formulation (also employing a cell-centered representation) and with the popular constrained transport method, where magnetic field components retain a staggered collocation inside the computational cell. Results obtained from two- and three-dimensional test problems indicate that the newly proposed scheme is robust, accurate and competitive with recent implementations of the constrained transport method while being considerably easier to implement in existing hydro codes.

*Key words:* Magnetohydrodynamics, Compressible Flow, Unsplit scheme, High-order Godunov method, Cell-centered method

---

## 1. Introduction

A primary aspect in building stable and robust Godunov type schemes for the numerical solution of the compressible magnetohydrodynamics (MHD) equations relies on an accurate way to control the solenoidal property of the magnetic field while preserving the conservation properties of the underlying physical laws. Failure to fulfill either requisite has been reported as a potential hassle leading to unphysical effects such as plasma acceleration in the direction of the field, incorrect jump conditions, wrong propagation speed of discontinuities and odd-even decoupling, see [26, 4]. A comprehensive body of literature has been dedicated to this subject and several strategies to enforce the  $\nabla \cdot \mathbf{B} = 0$  condition in Godunov-type codes have been proposed, see for example [28, 24, 25, 2, 26] and, more recently, [3, 18, 15, 23, 19]. The robustness of one method over another can be established on a practical base by extensive numerical testing, see [26, 4].

In a first class of schemes, the magnetic field is discretized as a cell-centered quantity and the usual formalism already developed for the Euler equation can be extended in a natural way. Cell-centered methods are appealing since the extensions to adaptive and/or unstructured grids are of straightforward implementation. Moreover, the same interpolation scheme and stencil used for the other hydrodynamic variables can be easily adapted since all quantities are discretized at the same spatial location, thus facilitating the extension to schemes possessing higher than second order accuracy. Unfortunately, numerical methods based on a cell-centered discretization do not naturally preserve Gauss's law of electromagnetism, even if  $\nabla \cdot \mathbf{B} = 0$

---

\*Corresponding Author

*Email addresses:* `mignone@ph.unito.it` (Andrea Mignone), `petros.tzeferacos@to.infn.it` (Petros Tzeferacos)

initially. In the approach suggested by Powell [21, 22], Gauss’s law for magnetism is discarded in the derivation of the MHD equations and the resulting system of hyperbolic laws is no longer conservative by the appearance of a source term proportional to  $\nabla \cdot \mathbf{B}$ . Although the source term should be physically zero at the continuous level, Powell showed that its inclusion changes the character of the equations by introducing an additional eighth wave corresponding to the propagation of jumps in the component of magnetic field normal to a given interface. A different approach is followed in the projection scheme [6, 28, 24, 9], where a Helmholtz-Hodge decomposition is applied to resolve  $\mathbf{B}$  as the sum of an irrotational and a solenoidal part, associated with scalar and vector potentials. A cleaning step allows to recover the divergence-free magnetic field by subtracting the unphysical contribution coming from the irrotational component at the extra cost of solving a Poisson equation. In the approach of Dedner et al. [12], the divergence-free constraint is enforced by solving a modified system of conservation laws where the induction equation is coupled to a generalized Lagrange multiplier. Dedner et al. showed that the choice of mixed hyperbolic/parabolic correction offers both propagation and dissipation of divergence errors with the maximal admissible characteristic speed, independently of the fluid velocity. This approach preserves the full conservation form of the original MHD system at the minimal cost of introducing one additional variable in the system and will be our scheme of choice. Finally, Torrilhon [27] (see also [1]) showed a general procedure to modify the inter-cell fluxes in the framework of a flux distribution scheme that preserves the value of a certain discrete divergence operator in each control volume.

A different strategy is followed in the constrained transport (CT) methods, originally devised by [13] and later built into the framework of shock-capturing Godunov methods by a number of investigators, e.g., [2, 3, 18, 15, 16]. In this class of schemes, the magnetic field has a staggered representation whereby the different components live on the face they are normal to. Hydrodynamic variables (density, velocity and pressure) retains their usual collocation at the cell center. CT schemes preserve the divergence-free condition to machine accuracy in an integral sense since the magnetic field is treated as a surface averaged quantity and thus more naturally updated using Stokes’ theorem. This evolutionary step involves the construction of a line-averaged electric field along the face edges, thereby requiring some sort of reconstruction or averaging of the electromotive force from the face center (where different components are usually available as face centered upwind Godunov fluxes) to the edges. A variety of different strategies have been suggested, including simple arithmetic averaging [2, 25], solution of 2-D Riemann problems [18, 14] or other somewhat more empirical approaches [15, 16, 17]. The staggered collocation of magnetic and electric field variables in CT schemes makes their extension to adaptive grids rather arduous and costly. Besides, significant efforts have to be spent in order to develop schemes with spatial accuracy of order higher than second. An alternative constrained transport method, based on the direct solution of the magnetic potential equation (thus avoiding staggered grids), has been presented by [23].

In the present work we propose a new fully unsplit Godunov scheme for multidimensional MHD, based on a combination of the Corner Transport Upwind of [8] and the mixed hyperbolic/parabolic divergence cleaning technique of [12] (CTU-GLM). The proposed scheme has second order accuracy in both space and time and adopts a cell-centered spatial collocation (no staggered mesh) of all flow variables, including the magnetic field. The scheme is fully conservative in mass, momentum, magnetic induction and energy and the divergence-free constraint is enforced via a mixed hyperbolic/parabolic correction which avoids the computational cost associated with an elliptic cleaning deriving from a Hodge projection. A variant of the scheme, which introduces divergence source terms breaking the conservative properties of some equations, is also presented. We assess the accuracy and robustness of the scheme by a direct quantitative comparison with the 8-wave formulation of [22] and the recently developed constrained transport method of [15, 16]. Other similar implementations may be found in [14, 17]. The comparison is conveniently handled using the PLUTO code for computational astrophysics [20] where both cell-centered and staggered-mesh implementations are available.

Our motivating efforts are driven by issues of simplicity, efficiency and flexibility. In this sense, the benefits offered by a method where all of the primary flow variables are discretized at the same spatial location considerably ease the extension to adaptive grids, to more complex physics and to schemes with higher than second order accuracy. The latter possibility will be explored in a companion paper.

## 2. The Constrained GLM-MHD Equations

In the approach of [12], the divergence constraint of the magnetic field (Gauss's law) is coupled to Faraday's equation by introducing a new scalar field function or generalized Lagrangian multiplier  $\psi$ . The second and third Maxwell's equations are thus replaced by

$$\left\{ \begin{array}{l} \nabla \cdot \mathbf{B} = 0, \\ \frac{\partial \mathbf{B}}{\partial t} = \nabla \times (\mathbf{v} \times \mathbf{B}), \end{array} \right. \implies \left\{ \begin{array}{l} \mathcal{D}(\psi) + \nabla \cdot \mathbf{B} = 0, \\ \frac{\partial \mathbf{B}}{\partial t} + \nabla \psi = \nabla \times (\mathbf{v} \times \mathbf{B}), \end{array} \right. \quad (1)$$

where  $\mathcal{D}$  is a linear differential operator. Dedner et al. built this approach into the MHD equations and showed that a satisfactory explicit approximation may be obtained by choosing a mixed hyperbolic/parabolic correction, according to which  $\mathcal{D}(\psi) = c_h^{-2} \partial_t^2 \psi + c_p^{-2} \partial_t \psi$  where  $c_h$  and  $c_p$  are constants. Direct manipulation of the modified Maxwell's equations (1) leads to the telegraph equation,

$$\frac{\partial^2 \psi}{\partial t^2} + \frac{c_h^2}{c_p^2} \frac{\partial \psi}{\partial t} = c_h^2 \Delta \psi, \quad (2)$$

which implies that divergence errors are propagated to the domain boundaries at finite speed  $c_h$  and decay with time and distance. The constant ratio  $c_h^2/c_p^2$ , which has the dimension of inverse time, sets the damping rate. In the limiting case of  $c_p \rightarrow \infty$ , one retrieves the simple hyperbolic correction and Eq. (2) reduces to an ordinary wave equation.

The GLM-Maxwell's equations (1) can be coupled to the equations of magnetohydrodynamics written in their conservative form. The resulting system is called the generalized Lagrange multiplier (GLM) formulation of the MHD equations (GLM-MHD) and is comprised of the following nine evolution equations:

$$\begin{aligned} \frac{\partial \rho}{\partial t} + \nabla \cdot (\rho \mathbf{v}) &= 0, \\ \frac{\partial(\rho \mathbf{v})}{\partial t} + \nabla \cdot \left[ \rho \mathbf{v} \mathbf{v}^T - \mathbf{B} \mathbf{B}^T + \mathbf{l} \left( p + \frac{\mathbf{B}^2}{2} \right) \right] &= 0, \\ \frac{\partial \mathbf{B}}{\partial t} + \nabla \cdot (\mathbf{v} \mathbf{B}^T - \mathbf{B} \mathbf{v}^T) + \nabla \psi &= 0, \\ \frac{\partial E}{\partial t} + \nabla \cdot \left[ \left( E + p + \frac{\mathbf{B}^2}{2} \right) \mathbf{v} - (\mathbf{v} \cdot \mathbf{B}) \mathbf{B} \right] &= 0, \\ \frac{\partial \psi}{\partial t} + c_h^2 \nabla \cdot \mathbf{B} &= -\frac{c_h^2}{c_p^2} \psi, \end{aligned} \quad (3)$$

where  $\rho$ ,  $\mathbf{v}$ ,  $p$  and  $\mathbf{B}$  are the mass density, velocity, gas pressure and magnetic field, respectively. Total energy  $E$  and gas pressure are related by the ideal gas law,  $E = p/(\Gamma - 1) + \rho \mathbf{v}^2/2 + \mathbf{B}^2/2$ , where  $\Gamma$  is the specific heat ratio. Notice that we have conveniently switched, using vector identities, to the divergence form of the induction equation, more appropriate for the cell-centered finite volume formalism. The constrained GLM-MHD equations (3) are hyperbolic and fully conservative in all flow variables with the exception of the unphysical scalar field  $\psi$  which satisfies a non-homogeneous equation with a source term. Divergence errors propagate with speed  $c_h$  independently of the flow velocity, thus avoiding accumulation in presence of stagnation points. The presence of the source term is responsible for damping divergence errors as they propagate.

Dedner et al. also considered a slightly different constrained formulation, in which the Lorentz force term in the MHD equations is directly derived from the GLM-Maxwell equations. In this case, the system (3) is extended by an additional source term on the right hand side, namely

$$\mathbf{S}_{GLM} = [0, -(\nabla \cdot \mathbf{B}) \mathbf{B}, \mathbf{0}, -\mathbf{B} \cdot \nabla \psi, 0]^T, \quad (4)$$

where the non-zero entries correspond to the momentum and energy equations. Dedner called the system (3) augmented with the source term (4) on its right hand side the *extended* GLM (EGLM) formulation of the MHD equations. Although the system breaks conservation of energy and momentum, it still holds some attractive features and we found it, in our experience, a more robust scheme in presence of strong discontinuity propagating through highly magnetized environments.

### 3. The CTU-GLM scheme

We now illustrate the detailed steps of our new cell-centered numerical scheme. The derivation is shown for the conservative GLM scheme, whereas modifications relevant to the EGLM formulation are described in §3.4.

We adopt a Cartesian system of coordinates and re-write the system of equations in (3) as

$$\frac{\partial}{\partial t} \begin{pmatrix} \rho \\ \rho v_d \\ B_d \\ E \\ \psi \end{pmatrix} + \sum_{l=x,y,z} \frac{\partial}{\partial l} \begin{pmatrix} \rho v_l \\ \rho v_d v_l - B_d B_l + \delta_{dl} (p + \mathbf{B}^2/2) \\ B_d v_l - B_l v_d + \delta_{dl} \psi \\ (E + p + \mathbf{B}^2/2) v_l - (\mathbf{v} \cdot \mathbf{B}) B_l \\ c_h^2 B_l \end{pmatrix} = \begin{pmatrix} 0 \\ 0 \\ 0 \\ 0 \\ -c_h^2/c_p^2 \psi \end{pmatrix}, \quad (5)$$

where  $d, l = x, y, z$  label the different component and flux contributions in the three directions while  $\delta_{dl}$  is the delta Kronecker symbol. The system of equations given in (5) is advanced in time by solving the homogeneous part separately from the source term contribution, in an operator-split fashion:

$$\mathbf{U}^{n+1} = \mathcal{S}^{\Delta t/2} \mathcal{A}^{\Delta t} \mathcal{S}^{\Delta t/2} \mathbf{U}^n \quad (6)$$

where  $\mathcal{A}$  and  $\mathcal{S}$  are the advection and source step operators separately described in §3.1 and §3.3, respectively.

#### 3.1. Advection Step

During the homogeneous step, we adopt a numerical discretization of (5) based on the corner transport upwind (CTU) method of [8]. For simplicity, we will assume hereafter an equally-spaced grid with computational cells centered in  $(x_i, y_j, z_k)$  having size  $\Delta x \times \Delta y \times \Delta z$ . For the sake of exposition, we omit the subscript  $(i, j, k)$  from cell centered quantities while keeping the half increment index notation when referring to the interfaces, e.g.,  $\rho_{j+\frac{1}{2}} \equiv \rho_{i,j+\frac{1}{2},k}$ . An explicit second order accurate discretization of Eqns. (5), based on a time-centered flux evaluation, reads

$$\mathbf{U}^{n+1} = \mathbf{U}^n - \Delta t^n \left[ \frac{\mathbf{F}_{i+\frac{1}{2}}^{n+\frac{1}{2}} - \mathbf{F}_{i-\frac{1}{2}}^{n+\frac{1}{2}}}{\Delta x} + \frac{\mathbf{G}_{j+\frac{1}{2}}^{n+\frac{1}{2}} - \mathbf{G}_{j-\frac{1}{2}}^{n+\frac{1}{2}}}{\Delta y} + \frac{\mathbf{H}_{k+\frac{1}{2}}^{n+\frac{1}{2}} - \mathbf{H}_{k-\frac{1}{2}}^{n+\frac{1}{2}}}{\Delta z} \right], \quad (7)$$

where  $\mathbf{U} = (\rho, \rho \mathbf{v}, \mathbf{B}, E, \psi)$  is the state vector of conservative variables. The expression in square brackets provides a conservative discretization of the divergence operator appearing in the original conservation laws with  $\mathbf{F}$ ,  $\mathbf{G}$  and  $\mathbf{H}$  being suitable numerical approximations to the flux contributions in (5) coming from the  $l = x, y, z$  directions, respectively. In the CTU approach, numerical fluxes are computed by solving a Riemann problem between suitable time-centered left and right states, i.e.,

$$\mathbf{F}_{i+\frac{1}{2}}^{n+\frac{1}{2}} = \mathcal{R} \left( \mathbf{V}_{i,+}^{n+\frac{1}{2}}, \mathbf{V}_{i+1,-}^{n+\frac{1}{2}} \right), \quad \mathbf{G}_{i+\frac{1}{2}}^{n+\frac{1}{2}} = \mathcal{R} \left( \mathbf{V}_{j,+}^{n+\frac{1}{2}}, \mathbf{V}_{j+1,-}^{n+\frac{1}{2}} \right), \quad \mathbf{H}_{i+\frac{1}{2}}^{n+\frac{1}{2}} = \mathcal{R} \left( \mathbf{V}_{k,+}^{n+\frac{1}{2}}, \mathbf{V}_{k+1,-}^{n+\frac{1}{2}} \right), \quad (8)$$

where  $\mathbf{V} = (\rho, \mathbf{v}, \mathbf{B}, p, \psi)^T$  is the state vector of primitive variables and  $\mathcal{R}(\cdot, \cdot)$  denotes the flux obtained by means of a Riemann solver, see §3.2. The corner-coupled states,  $\mathbf{V}_{i,+}^{n+\frac{1}{2}}$  and  $\mathbf{V}_{i+1,-}^{n+\frac{1}{2}}$ , are computed via a Taylor expansion consisting of an evolutionary step in the direction normal to a given interface (§3.1.1)

followed by a correction step involving transverse flux gradients (§3.1.2). The algorithm requires a total of 6 solution to the Riemann problem per zone per step.

The time increment  $\Delta t^n$  is computed via the Courant-Friedrichs-Levy (CFL) condition:

$$\Delta t^n = C_a \frac{\min(\Delta x, \Delta y, \Delta z)}{\max_{i,j,k} (|v_x| + c_{f,x}, |v_y| + c_{f,y}, |v_z| + c_{f,z})}, \quad (9)$$

where the maximum and minimum are taken over all zones and  $c_{f,x}, c_{f,y}, c_{f,z}$  are the fast magneto-sonic speeds in the three directions, see §3.1.1.  $C_a$  is the Courant number and, for the 6-solve CTU presented here, is restricted to  $C_a < 1$  in two dimensions and  $C_a < 1/2$  in three dimensions.

### 3.1.1. Normal Predictors

During the computation of the normal predictors, we take advantage of the primitive (or quasi-linear) form of the equations. By discarding contributions from  $y$  and  $z$  and considering the reconstruction process in the  $x$  direction only, one has

$$\frac{\partial \mathbf{V}}{\partial t} + \mathbf{A}_x \frac{\partial \mathbf{V}}{\partial x} = \mathbf{S}_{B_x} \frac{\partial B_x}{\partial x} + \mathbf{S}_\psi \frac{\partial \psi}{\partial x}, \quad (10)$$

where the  $9 \times 9$  matrix

$$\mathbf{A}_x = \begin{pmatrix} v_x & \rho & 0 & 0 & 0 & 0 & 0 & 0 & 0 \\ 0 & v_x & 0 & 0 & 0 & B_y/\rho & B_z/\rho & 1/\rho & 0 \\ 0 & 0 & v_x & 0 & 0 & -B_x/\rho & 0 & 0 & 0 \\ 0 & 0 & 0 & v_x & 0 & 0 & -B_x/\rho & 0 & 0 \\ 0 & 0 & 0 & 0 & 0 & 0 & 0 & 0 & 1 \\ 0 & B_y & -B_x & 0 & 0 & v_x & 0 & 0 & 0 \\ 0 & B_z & 0 & -B_x & 0 & 0 & v_x & 0 & 0 \\ 0 & \Gamma p & 0 & 0 & 0 & 0 & 0 & v_x & 0 \\ 0 & 0 & 0 & 0 & c_h^2 & 0 & 0 & 0 & 0 \end{pmatrix}, \quad (11)$$

is the usual matrix of the MHD equations in primitive form plus the addition of a fifth row and a ninth column. The source terms  $\mathbf{S}_{B_x}$  and  $\mathbf{S}_\psi$  are of crucial importance for the accuracy of the scheme in multi-dimensions [9, 15, 17] and take the form

$$\mathbf{S}_{B_x} = \left[ 0, \frac{B_x}{\rho}, \frac{B_y}{\rho}, \frac{B_z}{\rho}, 0, v_y, v_z, -(\Gamma - 1)\mathbf{v} \cdot \mathbf{B}, 0 \right]^T, \quad \mathbf{S}_\psi = \left[ 0, 0, 0, 0, 0, (\Gamma - 1)B_x, 0 \right]^T. \quad (12)$$

The matrix  $\mathbf{A}_x$  of the quasi-linear form is diagonalizable with the same eigenvalues as the ordinary MHD equations plus two new additional entries  $c_h$  and  $-c_h$ , for a total of 9 characteristic waves:

$$\lambda^{1,9} = \mp c_h, \quad \lambda^{2,8} = v_x \mp c_f, \quad \lambda^{3,7} = v_x \mp c_a, \quad \lambda^{4,6} = v_x \mp c_s, \quad \lambda^5 = v_x, \quad (13)$$

where

$$c_{f,s} = \sqrt{\frac{1}{2\rho} \left( \Gamma p + |\mathbf{B}|^2 \pm \sqrt{(\Gamma p + |\mathbf{B}|^2)^2 - 4\Gamma p B_x^2} \right)}, \quad c_a = \frac{|B_x|}{\sqrt{\rho}}, \quad (14)$$

are the fast magneto-sonic ( $c_f$  with the + sign), slow magneto-sonic ( $c_s$  with the - sign) and Alfvén velocities. The two additional modes  $\pm c_h$  are decoupled from the remaining ones and corresponds to waves

carrying jumps in  $B_x$  and  $\psi$ . The constant  $c_h$  gives the speed of propagation of local divergence errors and is chosen to be the maximum speed compatible with the time step restriction, in other words

$$c_h = \max_{i,j,k} (|v_x| + c_{f,x}, |v_y| + c_{f,y}, |v_z| + c_{f,z}) , \quad (15)$$

Finally, the corresponding left ( $\mathbf{l}^k$ ) and right ( $\mathbf{r}^k$ ) eigenvectors are given in Appendix A.

Using the characteristic decomposition of the quasi-linear form (10), we extrapolate  $\mathbf{V}(x_i, t^n)$  from the cell center to the edges  $x_{i\pm\frac{1}{2}}$  for a time increment  $\Delta t^n/2$ . During this step we only consider the contribution of those waves traveling from the center to the given interface and discard any interaction between neighbor cells. The resulting construction yields the normal predictors

$$\mathbf{V}_{i,\pm}^* = \mathbf{V}_i^n + \frac{1}{2} \sum_{k:\lambda_i^k \geq 0} \left( \pm 1 - \frac{\lambda_i^k \Delta t^n}{\Delta x} \right) \Delta \mathbf{V}_i^k + \frac{\Delta t^n}{2\Delta x} (\mathbf{S}_{B_x,i}^n \Delta B_x + \mathbf{S}_{\psi,i}^n \Delta \psi) , \quad (16)$$

where only positive waves ( $\lambda_i^k > 0$ ,  $k = 1, \dots, 9$ ) contribute to the left of the  $i + \frac{1}{2}$  interface ( $i, +$ ) while only negative waves ( $\lambda_i^k < 0$ ) are considered to the right of the  $i - \frac{1}{2}$  interface ( $i, -$ ). The undivided differences  $\Delta B_x$  and  $\Delta \psi$  may be computed using a standard centered finite difference approximation. The jump contribution from the  $k$ -th characteristic field is denoted with  $\Delta \mathbf{V}_i^k = \Delta w_i^k \mathbf{r}_i^k$  where  $\mathbf{r}_i^k$  is the corresponding right eigenvector and  $\Delta w_i^k$  is a limited slope in the  $k$ -th characteristic variable,

$$\Delta w_i^k = \text{Lim} \left( \mathbf{l}_i^k \cdot \Delta \mathbf{V}_{i+\frac{1}{2}}^n, \mathbf{l}_i^k \cdot \Delta \mathbf{V}_{i-\frac{1}{2}}^n \right) , \quad (17)$$

where  $\Delta \mathbf{V}_{i\pm\frac{1}{2}}^n = \pm (\mathbf{V}_{i\pm 1}^n - \mathbf{V}_i^n)$ ,  $\mathbf{l}_i^k$  is the  $k$ -th primitive left eigenvector and  $\text{Lim}(\cdot, \cdot)$  is a limiter function, e.g.

$$\text{Lim}(\delta_-, \delta_+) = \frac{\text{sign}(\delta_-) + \text{sign}(\delta_+)}{2} \min \left( \beta |\delta_-|, \beta |\delta_+|, \frac{\delta_- + \delta_+}{2} \right) . \quad (18)$$

Usually taking  $\beta = 2$  gives the largest compression. However, for problems involving strong shocks, we found setting  $\beta = 1$  for nonlinear fields (fast and slow shocks) and  $\beta = 2$  for the linear fields to give a more robust recipe.

### 3.1.2. Transverse Predictors

Once the normal predictor states have been computed, we solve a Riemann problem at constant  $y$ - and  $z$ - faces to obtain the transverse fluxes, e.g.,

$$\mathbf{G}_{j+\frac{1}{2}}^* = \mathcal{R}(\mathbf{V}_{j,+}^*, \mathbf{V}_{j+1,-}^*) , \quad \mathbf{H}_{k+\frac{1}{2}}^* = \mathcal{R}(\mathbf{V}_{k,+}^*, \mathbf{V}_{k+1,-}^*) , \quad (19)$$

where left and right states have been computed during the normal predictor stages in the  $y$  and  $z$  direction. The solution of the Riemann problem follows the guidelines illustrated in §3.2, where the linear sub-system formed by the longitudinal magnetic field component and the Lagrange multiplier is preliminary solved before a standard 7-wave Riemann solver is applied. Transverse flux gradients are then added to the normal predictors (16) once they are transformed back to conservative variables. This yields the corner coupled states:

$$\mathbf{U}_{i\pm\frac{1}{2}}^{n+\frac{1}{2}} = \mathbf{U}_{i\pm\frac{1}{2}}^* - \frac{\Delta t}{2} \left( \frac{\mathbf{G}_{j+\frac{1}{2}}^* - \mathbf{G}_{j-\frac{1}{2}}^*}{\Delta y} + \frac{\mathbf{H}_{k+\frac{1}{2}}^* - \mathbf{H}_{k-\frac{1}{2}}^*}{\Delta z} \right) , \quad (20)$$

where  $\mathbf{U}^*$  is obtained by converting  $\mathbf{V}^*$  to conservative variables.

We recall that the starting point in the derivation of Eq. (20) may be viewed, in its simplest form, as a first order Taylor expansion around the cell center  $(x_i, t^n)$ ,

$$\mathbf{U}_{i\pm\frac{1}{2}}^{n+\frac{1}{2}} \approx \mathbf{U}_i^n \pm \frac{\partial \mathbf{U}_i^n}{\partial x} \frac{\Delta x}{2} + \frac{\partial \mathbf{U}_i^n}{\partial t} \frac{\Delta t}{2} \approx \left( \mathbf{U}_i^n \pm \frac{\partial \mathbf{U}_i^n}{\partial x} \frac{\Delta x}{2} - \frac{\Delta t}{2} \frac{\partial \mathbf{F}_i^n}{\partial x} \right) - \frac{\Delta t}{2} \left( \frac{\partial \mathbf{G}_i^*}{\partial y} + \frac{\partial \mathbf{H}_i^*}{\partial z} \right) , \quad (21)$$

where the temporal derivative  $\partial\mathbf{U}/\partial t$  has been replaced, in the second expression, by taking advantage of the original conservation law and the different terms have been grouped according to the step in which they are computed (i.e., Eq 16 and Eq 20). In this perspective, the input states entering in the computation of the transverse fluxes (19) may be slightly modified by  $O(\Delta t^2)$  in order to more accurately represent the  $\nabla \cdot \mathbf{B}$  term in the construction of the scalar multiplier  $\psi$ . To better understand this minor correction, we rewrite the  $\psi$  component of the interface states (20) in 2D using, for the sake of simplicity, a simple MUSCL-Hancock step during the normal predictor:

$$\psi_{\pm}^{n+\frac{1}{2}} = \psi^n \pm \frac{\Delta\psi^n}{2} - \frac{c_h^2 \Delta t}{2} \left[ \frac{\Delta B_x^n}{\Delta x} + \frac{B_{y,j+\frac{1}{2}}^* - B_{y,j-\frac{1}{2}}^*}{\Delta y} \right]. \quad (22)$$

Clearly, the multidimensional terms approximating  $\nabla \cdot \mathbf{B}$  in the square bracket of Eq. (22) split into a normal ( $\Delta B_x^n$ ) and a transverse ( $B_{y,j+\frac{1}{2}}^* - B_{y,j-\frac{1}{2}}^*$ ) directional contribution. Since the first one is taken at time level  $n$  while the second term comes from solving a Riemann problem between normal predictors in the  $y$  direction (extrapolated a  $t^n + \Delta t^n/2$ ), these contributions are not taken at the same time level but are spaced by  $\Delta t^n/2$ . In practice, from the tests included here and several others we found evidence that a better balance is achieved if one replaces, in the input states of (19), the longitudinal field component with its interpolated value at time level  $n$ , i.e.,  $B_{y,j,\pm}^* \rightarrow B_y^n \pm \Delta B_y^n/2$  (or, equivalently with the value obtained by setting  $\Delta t = 0$  in Eq. 16). Note that this is a second-order correction that does not alter the accuracy of the scheme and only affects the solution of the Riemann problem in computing the transverse fluxes (19) but does not concern the definitions of the normal predictors. Although this is not an essential step, it was found to improve the accuracy in the numerical tests presented in §4.

### 3.2. Solving the Riemann Problem

In the case of the GLM-MHD equations, left and right input states to the Riemann solver  $\mathcal{R}(\cdot, \cdot)$  bring a set of 9 jumps propagating along the 7 standard characteristic MHD waves (i.e. fast, slow, rotational pairs and one entropy modes) as well as 2 additional modes carrying jumps only in the normal (longitudinal) component of  $\mathbf{B}$  and  $\psi$ . Nonetheless, when solving a one-dimensional Riemann problem at a zone interface (say the  $x$  direction), these additional waves are decoupled from the remaining ones and are described by the  $2 \times 2$  linear hyperbolic system

$$\begin{cases} \frac{\partial B_x}{\partial t} = -\frac{\partial \psi}{\partial x} \\ \frac{\partial \psi}{\partial t} = -c_h^2 \frac{\partial B_x}{\partial x}. \end{cases} \quad (23)$$

For a generic pair of left and right input states  $(B_{x,L}, \psi_L)$  and  $(B_{x,R}, \psi_R)$ , the Godunov flux of the system (23) can be computed exactly as

$$B_x^* = \frac{B_{x,L} + B_{x,R}}{2} - \frac{1}{2c_h} (\psi_R - \psi_L), \quad \psi^* = \frac{\psi_L + \psi_R}{2} - \frac{c_h}{2} (B_{x,R} - B_{x,L}). \quad (24)$$

This allows to carry out the solution of the  $2 \times 2$  linear Riemann problem separately before using any standard 7-wave Riemann solver for the one-dimensional MHD equations. The longitudinal component of the magnetic field  $B_x^*$ , preliminary computed with (24), enters hence the ordinary Riemann flux computation as a constant parameter.

In other words, given the arbitrary left and right states  $\mathbf{V}_L$  and  $\mathbf{V}_R$ , input to the Riemann problem, we compute

$$\mathcal{R}(\mathbf{V}_L, \mathbf{V}_R) = \mathcal{R}_7(\mathbf{V}_L^*, \mathbf{V}_R^*) \quad (25)$$

where  $\mathbf{V}_S^*$  ( $S = L, R$ ) is the same as  $\mathbf{V}_S$  with  $(B_{x,S}, \psi_S)$  replaced by  $(B_x^*, \psi^*)$  and  $\mathcal{R}_7$  is a standard 7-wave Riemann solver. In this work, we will employ the linearized Riemann solver of Roe, in the version of [7].

### 3.3. Source Step

During the source step we solve the initial value problem given by the last of equations (3) without the  $\nabla \cdot \mathbf{B}$  term, that is,

$$\frac{\partial \psi}{\partial t} = -\frac{c_h^2}{c_p^2} \psi, \quad (26)$$

supplemented with the initial condition  $\psi^{(0)}$  given by the output of the most recent step. The constant  $c_p^2$  has the dimension of length squared over time and thus can be regarded as a diffusion coefficient. Dedner et al. prescribe an optimal value  $c_p^2/c_h = 0.18$  independently of the mesh spacing; however, we suspect this definition to be incomplete, since  $c_p^2/c_h$  has the dimension of length and thus it is *not* a dimensionless quantity. Our numerical experiments indicate that divergence errors are minimized when the parameter  $\alpha = \Delta h c_h / c_p^2$  (where  $\Delta h = \min(\Delta x, \Delta y, \Delta z)$ ) lies in the range  $\alpha \in [0, 1]$ , depending on the particular problem. In first approximation this value can be regarded as grid-independent although we have verified a weak tendency to decrease as the mesh thickens. Using the definition of  $\alpha$ , Eq. (26) can be integrated exactly for a time increment  $\Delta t^n$ , yielding

$$\psi^{(\Delta t^n)} = \psi^{(0)} \exp\left(-\alpha \frac{c_h}{\Delta h / \Delta t}\right), \quad \text{with} \quad \alpha = \Delta h \frac{c_h}{c_p^2}. \quad (27)$$

Note that, when  $c_h$  is chosen using Eq. (15), the argument of the exponential becomes simply  $(-C_a \alpha)$ . Finally, we comment out that the dimensionless  $\alpha$  parameter can be regarded as the ratio of the diffusive and advective time scales, i.e.,  $\alpha = \Delta t_d / \Delta t_a$ , where  $\Delta t_d = \Delta h^2 / c_p^2$  and  $\Delta t_a = \Delta h / c_h$ .

### 3.4. Modifications for the Extended GLM (EGLM) formulation

The extended GLM-MHD (EGLM-MHD) equations may be derived from the primitive MHD equations rather than the conservative ones, [12]. In this approach, the divergence part of the Lorentz force is added to the momentum flux and an additional source term, given by (4), is introduced into the system. The construction of the normal predictor states carried out in §3.1.1 remains the same with the exception of the source terms (12) which must be replaced by

$$\mathbf{S}_{B_x} = [0, 0, 0, 0, 0, v_y, v_z, -(\Gamma - 1) \mathbf{v} \cdot \mathbf{B}, 0]^T, \quad \mathbf{S}_\psi = \mathbf{0}. \quad (28)$$

Since the corner coupled states in Eq. (20) are obtained in conservative variables, they must also be augmented with the source term contribution (Eq. 4) and thus replaced by

$$\mathbf{U}_{i \pm \frac{1}{2}}^{n+\frac{1}{2}} \rightarrow \mathbf{U}_{i \pm \frac{1}{2}}^{n+\frac{1}{2}} + \frac{\Delta t}{2} (\mathbf{S}_{EGLM,y}^n + \mathbf{S}_{EGLM,z}^n). \quad (29)$$

Likewise, the final update Eq. (7) becomes

$$\mathbf{U}^{n+1} \rightarrow \mathbf{U}^{n+1} + \Delta t (\mathbf{S}_{EGLM,x}^{n+\frac{1}{2}} + \mathbf{S}_{EGLM,y}^{n+\frac{1}{2}} + \mathbf{S}_{EGLM,z}^{n+\frac{1}{2}}). \quad (30)$$

In Eq. (29) and (30) we have split the source term into contributions coming from the derivatives in the  $x$ ,  $y$  and  $z$  directions. For each term we take advantage of the upwind fluxes computed in the corresponding direction during the Riemann solver step. For example, during the  $y$ -sweep we compute the momentum and energy sources in  $\mathbf{S}_{EGLM,y}$  as

$$-\mathbf{B} \frac{\partial B_y}{\partial y} \approx -\mathbf{B} \left( \frac{B_{y,j+\frac{1}{2}}^* - B_{y,j-\frac{1}{2}}^*}{\Delta y} \right), \quad -B_y \frac{\partial \psi}{\partial y} \approx -B_y \left( \frac{\psi_{j+\frac{1}{2}}^* - \psi_{j-\frac{1}{2}}^*}{\Delta y} \right), \quad (31)$$

where  $B_y^*$  and  $\psi^*$  follows from the solution of the linear  $2 \times 2$  Riemann problem (24). The cell-centered magnetic field is evaluated at  $t^n$  for the computation of the corner coupled states (29) and by averaging to cell-center the final interface values for the final update, Eq. (30).

## 4. Numerical Tests

We now proceed to a direct verification of the CTU-GLM and CTU-EGLM algorithms developed in the previous sections. A test suite of standard two- and three-dimensional MHD problems has been selected in order to monitor and quantify the accuracy of the proposed schemes. For the sake of comparison, we extend the verification process to other two well known methods, namely, Powell's eight wave formulation [22] based on a cell-centered approach and the constrained transport (CT) scheme of [15, 16] using a staggered formulation. The four selected algorithms, "GLM", "EGLM", "8W" and "CT", have been built into the CTU methodology and have been implemented in the current distribution of the PLUTO code for astrophysical gas-dynamics [20] available at <http://plutocode.to.astro.it>. Adopting the same numerical framework provides a practical way for a convenient and extensive inter-scheme comparison.

In the following test problems the scalar field function  $\psi$  will be always initialized to zero and thus omitted from the definition of the initial conditions. Moreover, unless otherwise stated, the specific heat ratio will be set to  $\Gamma = 5/3$  and the default Courant number is set to  $C_a = 0.8$  in two dimensions and  $C_a = 0.4$  in three dimensions. Errors for any flow quantity  $Q$  are computed using the  $L_1$  discrete norm defined by

$$\epsilon_1(Q) = \frac{1}{N_x N_y N_z} \sum_{i,j,k} |Q_{i,j,k} - Q_{i,j,k}^{\text{ref}}| \quad (32)$$

where  $N_x$ ,  $N_y$  and  $N_z$  are the number of points in the three directions,  $Q_{i,j,k}^{\text{ref}}$  is a reference solution and the summation extends to all grid zones.

### 4.1. Propagation of Circularly polarized Alfvén Waves

Circularly polarized Alfvén waves are an exact nonlinear solution of the compressible MHD equations thus providing an excellent code benchmark. For a planar wave propagating along the  $x$  direction with angular frequency  $\omega$  and wave number  $k$ , the transverse components of velocity and magnetic fields trace circles in the  $yz$  plane and the solution can be written as

$$\begin{pmatrix} v_x \\ v_y \\ v_z \end{pmatrix} = \begin{pmatrix} v_{0x} \\ v_{0y} + A \sin \phi \\ v_{0z} + A \cos \phi \end{pmatrix}, \quad \begin{pmatrix} B_x \\ B_y \\ B_z \end{pmatrix} = \begin{pmatrix} c_a \sqrt{\rho} \\ \mp \sqrt{\rho} A \sin \phi \\ \mp \sqrt{\rho} A \cos \phi \end{pmatrix}, \quad (33)$$

where  $\phi = kx - \omega t$ ,  $\omega/k = v_{0x} \pm c_a$  is the corresponding phase velocity ( $c_a = 1$  is the Alfvén speed) and  $A = 1/10$  is the wave amplitude. The plus or minus sign corresponds to right or left propagating waves, respectively. The constants  $v_{0x}, v_{0y}, v_{0z}$  give the translational velocity components in the three directions. Density and pressure remain constant and equal to their initial values  $\rho_0 = 1$  and  $p_0 = 0.1$  since torsional Alfvén waves do not involve any compression.

Here we consider a rotated version of the one-dimensional solution given by (33) and specify the orientation of the wave vector  $\mathbf{k} = (k_x, k_y, k_z)$  in a three dimensional space  $x, y, z$  through the angles  $\alpha$  and  $\beta$  such that

$$\tan \alpha = \frac{k_y}{k_x}, \quad \tan \beta = \frac{k_z}{k_x}. \quad (34)$$

The full 3D solution is then recovered by rotating the original one dimensional frame by an angle  $\gamma = \tan^{-1}(\cos \alpha \tan \beta)$  around the  $y$  axis and subsequently by an angle  $\alpha$  around the  $z$  axis. The resulting transformation leaves scalar quantities invariant and produce vectors rotation  $\mathbf{q} \rightarrow \mathbf{R}_{\gamma\alpha}\mathbf{q}$ , where

$$\mathbf{R}_{\gamma\alpha} = \begin{pmatrix} \cos \alpha \cos \gamma & -\sin \alpha & -\cos \alpha \sin \gamma \\ \sin \alpha \cos \gamma & \cos \alpha & -\sin \alpha \sin \gamma \\ \sin \gamma & 0 & \cos \gamma \end{pmatrix}, \quad \mathbf{R}_{\gamma\alpha}^{-1} = \begin{pmatrix} \cos \alpha \cos \gamma & \sin \alpha \cos \gamma & \sin \gamma \\ -\sin \alpha & \cos \alpha & 0 \\ -\cos \alpha \sin \gamma & -\sin \alpha \sin \gamma & \cos \gamma \end{pmatrix}, \quad (35)$$

are the rotation matrix and its inverse whereas  $\mathbf{q}$  is a three-dimensional vector. Note that  $\phi$  is now given by  $\phi = \mathbf{k} \cdot \mathbf{x} - \omega t$  where  $\omega = |\mathbf{k}|(v_{0x} \pm c_a)$  and

$$|\mathbf{k}| = k_x \sqrt{1 + \tan^2 \alpha + \tan^2 \beta} \quad (36)$$

is the wavenumber corresponding to a wavelength  $\lambda = 2\pi/|\mathbf{k}|$  and period  $T = 2\pi/\omega$ .

In order to ensure correct periodicity we assume, without loss of generality,  $k_x = 2\pi$  and pattern the computational domain such that one wave period is prescribed in each grid direction, i.e.,  $x \in [0, 1]$ ,  $y \in [0, 1/\tan \alpha]$  and  $z \in [0, 1/\tan \beta]$ . Also, for the tests discussed here, we consider standing waves and thus set  $v_{0x} = v_{0y} = v_{0z} = 0$ . With these definitions the wave returns into the original position after one period  $T = \lambda/c_a$  with

$$T = \frac{1}{\sqrt{1 + \tan^2 \alpha + \tan^2 \beta}}. \quad (37)$$

#### 4.1.1. Two-Dimensional Propagation

Table 1: Errors (in  $L_1$  norm) and orders of accuracy for the two and three-dimensional circularly polarized Alfvén wave tests. The first and second columns refer to the numerical scheme and the number of points in the  $x$  direction. Columns 3-4 and 5-6 show the result obtained in the 2D problem with Courant number of  $C_a = 0.8$  and  $C_a = 0.4$ , respectively. The last two columns corresponds to the three dimensional case.

Scheme	$N_x$	2D, $C_a = 0.8$		2D, $C_a = 0.4$		3D, $C_a = 0.4$	
		$L_1$ Error	$L_1$ order	$L_1$ Error	$L_1$ order	$L_1$ Error	$L_1$ order
GLM	16	2.46E-002	-	2.60E-002	-	3.19E-002	-
	32	4.56E-003	2.43	5.17E-003	2.33	5.66E-003	2.50
	64	1.16E-003	1.97	1.27E-003	2.03	1.15E-003	2.30
	128	3.19E-004	1.87	3.02E-004	2.07	3.03E-004	1.92
	256	8.48E-005	1.91	7.01E-005	2.11	8.05E-005	1.91
CT	16	2.54E-002	-	2.79E-002	-	3.44E-002	-
	32	4.96E-003	2.36	7.09E-003	1.98	5.57E-003	2.63
	64	1.16E-003	2.09	1.90E-003	1.90	1.18E-003	2.24
	128	2.76E-004	2.08	4.25E-004	2.16	3.24E-004	1.86
	256	6.73E-005	2.04	9.32E-005	2.19	9.67E-005	1.75
8W	16	2.60E-002	-	2.81E-002	-	3.37E-002	-
	32	5.19E-003	2.32	7.28E-003	1.95	5.44E-003	2.63
	64	1.22E-003	2.09	1.88E-003	1.95	1.37E-003	1.99
	128	2.96E-004	2.05	4.02E-004	2.22	3.45E-004	1.99
	256	7.29E-005	2.02	8.40E-005	2.26	8.79E-005	1.97

We begin by considering two dimensional propagation choosing  $\tan \alpha = 2$ ,  $\beta = 0$  in accordance with [18, 15, 17]. Computations are carried out for exactly one wave period ( $t = T = 1/\sqrt{5}$ ) on the computational box  $[0, 1] \times [0, 1/2]$  with  $N_x \times N_y$  points, where  $N_y = N_x/2$ . Errors, computed as  $\sqrt{\epsilon_1(B_x)^2 + \epsilon_1(B_y)^2 + \epsilon_1(B_z)^2}$ , are reported in Table 1 and plotted as function of the mesh size,  $N_x = 16, \dots, 256$ , in the left panel of Fig 1.

Selected schemes (CT, GLM and 8W) produce comparable errors and show essentially second-order accuracy. We notice that decreasing the Courant number to  $C_a = 0.4$  has the effect of slightly reducing the errors for GLM at large resolution but not for CT and 8W. From Table 1, in fact, one can see that, when  $N_x = 256$ , the error is reduced from  $\sim 8.5 \cdot 10^{-5}$  to  $\sim 7 \cdot 10^{-5}$  for GLM, while it grows from  $6.7 \cdot 10^{-5}$  to  $9.3 \cdot 10^{-5}$  for the CT scheme.

We have found that the solution is very weakly dependent on the  $\alpha$  parameter and the errors are minimized when  $\alpha = 0$ . Besides, we repeated the computations with the EGLM formulation and observed essentially the same level of accuracy with no particular improvement over GLM.

#### 4.1.2. Three-Dimensional Propagation

In three dimensions we follow [16] and set  $\tan \alpha = \tan \beta = 2$  so that the resulting computational box is given by  $x \in [0, 1]$ ,  $y, z \in [0, 1/2]$  discretized on  $N_x \times N_x/2 \times N_x/2$  grid points. Computations are followed for one wave period ( $T = 1/3$ ) and repeated, with  $C_a = 0.4$ , on increasingly finer grids corresponding to  $N_x = 16, 32, 64, 128, 256$ . The right panel in Figure 1 shows that all schemes meet the expected order of accuracy providing comparable errors, as found in the two-dimensional case. A more quantitative comparison can be made by inspecting the last two columns of Table 1, where one can see that GLM performs slightly better than the other schemes.

#### 4.2. Nonlinear smooth flow

In the next example we consider the evolution of a fully nonlinear smooth flow where, unlike the previous example, all waves (linear and nonlinear) are triggered. Following [27, 1] we specify a periodic computational box in Cartesian coordinates, spanning from  $-1$  to  $1$  in the  $x$  and  $y$  directions with initial conditions given by

$$\begin{aligned} \rho &= \frac{3}{2} + \frac{1}{2} \sin(\pi x) + \frac{1}{4} \cos(\pi y), \\ (v_x, v_y) &= \left[ 1 + \frac{1}{2} \sin(\pi y) + \frac{1}{4} \cos(\pi x), 1 + \frac{1}{4} \sin(\pi x) + \frac{1}{2} \cos(\pi y) \right], \\ (B_x, B_y) &= \left( \frac{1}{2}, 1 \right), \end{aligned} \quad (38)$$

where  $p = 1/4$ , while  $v_z = B_z = 0$ . Integration terminates at  $t = 0.2$ , before the formation of any discontinuous feature. A resolution study is carried out for all schemes and compared to a reference solution obtained on  $2048^2$  zones with the CT scheme. The error, shown in Fig. (2) as a function of the number of cells, is computed as a quadratic mean of the  $L_1$  norm errors (given by Eq. 32) of the primitive variables. All schemes are second-order accurate with comparable errors, with the GLM approach giving slightly better results than the others at the largest resolution (256 zones).

#### 4.3. Shock Tube Problems

One dimensional shock tubes have proven to be valuable benchmarks in order to assess the ability of the scheme to capture both continuous and discontinuous flow features. The rotated multidimensional versions considered in the following may be used to check the strength of the numerical method in preserving the original planar symmetry through an oblique propagation.

##### 4.3.1. Two-dimensional shock tube

In the first shock tube, taken from [26], we consider an initial discontinuity with left and right states given by  $(\rho, v_1, v_2, B_1, B_2, p)_L = (1, 10, 0, 5/\sqrt{4\pi}, 5/\sqrt{4\pi}, 20)$  and  $(\rho, v_1, v_2, B_1, B_2, p)_R = (1, -10, 0, 5/\sqrt{4\pi}, 5/\sqrt{4\pi}, 1)$  respectively. The subscripts “1” and “2” give the directions perpendicular and parallel to the initial discontinuity. The initial condition is then rotated on a Cartesian grid  $(x, y)$  using the transformation defined by Eq. (35) with  $\alpha = \tan^{-1} 2$  and  $\beta = \gamma = 0$ .

Since the magnetic field is initially uniform,  $\nabla \cdot \mathbf{B} = 0$  is trivially ensured at  $t = 0$ . The computational domain spans from 0 to 1 in the  $x$  direction and from 0 to  $2/N_x$  in the  $y$  direction with  $N_x \times 2$  computational zones. Outflow boundaries are set at the rightmost and leftmost sides of the box whereas for any flow variables  $q$  at the upper and lower boundaries we impose the translational invariance  $q(i, j) = q(i \pm \delta i, j \pm \delta j)$  where  $(\delta i, \delta j) = (2, -1)$  with the plus (minus) sign holding at the upper (lower) boundary. Computations terminate before the fast shocks reach the boundaries, at  $t = 0.08 \cos \alpha$ .

Table 2: One dimensional  $L_1$  ( $\times 10^{-2}$ ) norm error for the two-dimensional shock tube.

	$\rho$	$V_1$	$V_2$	$B_1$	$B_2$	$p$
8W	2.7	8.6	1.9	<b>9.6</b>	6.2	94.5
CT	2.6	8.5	1.5	<b>0.4</b>	4.7	93.0
GLM	2.6	8.4	1.4	<b>0.4</b>	4.3	90.5
EGLM	3.2	8.3	1.3	<b>0.4</b>	5.1	96.4

Fig 3 shows the primitive variable profiles obtained with the conservative GLM-MHD scheme. The resulting wave pattern is comprised of two outermost fast shocks (at  $x_1 \sim 0.12$  and  $x_1 \sim 0.86$ ) enclosing two slow magneto-sonic waves and a contact mode at  $x_1 \sim 0.56$ . We see that all discontinuities are captured correctly although some spurious oscillations are visible in the transverse velocity profile in proximity of the fast shocks. Similar features are also evident in the paper by Tóth [26] and with the CT scheme (not shown here).

We have repeated the same test with the four different schemes described at the beginning of this section and compared the results against a one-dimensional reference solution obtained at higher resolution (1024 cells) up to  $t = 0.08$ . Table 2 gives the errors, using the one-dimensional  $L_1$  norm, of the primitive variables for the 8W, CT, GLM and EGLM schemes. While errors in density, velocity and pressure are very similar for all schemes, the longitudinal component of the magnetic field ( $B_1$ ) shows substantially large deviations with the 8W scheme. This is further illustrated in Fig 4 where, in accordance with [26], we find that the 8-wave formulation results in erroneous jump conditions in the normal component of the field. On the other hand, both the GLM and the non conservative EGLM schemes behave as well as CT on this particular test without producing spurious jump conditions.

Finally, in the left panel in Fig. 7 we plot, as a function of  $\alpha$ , the  $L_1$  norm errors in  $B_1$  at different resolutions,  $N_x = 128, 256, 512$ , for both the GLM (black) and EGLM (red) formulations. The plots show a weak dependence on the  $\alpha$  parameter and errors are minimized for  $\alpha \approx 0.5$ , independently of the mesh resolution, for both schemes. Also, owing to the presence of shock waves, the order of convergence is approximately one.

#### 4.3.2. Three-dimensional shock tube

For the three dimensional version we follow [16] and set the initial left and right states to

$$\begin{cases} \mathbf{V}_L &= \left( 1.08, 1.2, 0.01, 0.5, \frac{2}{\sqrt{4\pi}}, \frac{3.6}{\sqrt{4\pi}}, \frac{2}{\sqrt{4\pi}}, 0.95 \right)^T & \text{for } x_1 < 0, \\ \mathbf{V}_R &= \left( 1, 0, 0, 0, \frac{2}{\sqrt{4\pi}}, \frac{4}{\sqrt{4\pi}}, \frac{2}{\sqrt{4\pi}}, 1 \right)^T & \text{for } x_1 > 0, \end{cases} \quad (39)$$

where  $\mathbf{V} = (\rho, v_1, v_2, v_3, B_1, B_2, B_3, p)$  is the vector of primitive variables. The coordinate transformation used for the 3D rotation is given by Eq. (35) where the rotation angles  $\alpha$  and  $\beta$  are chosen in such a way that an integer shift of cells satisfies, for any flow quantities  $q$ , the translational invariance expressed by  $q(\mathbf{x} + \mathbf{s}) = q(\mathbf{x})$ , where  $\mathbf{s}$  is a Cartesian vector orthogonal to  $\mathbf{x}_1$  and thus  $x_1(\mathbf{x} + \mathbf{s}) = x_1(\mathbf{x})$ . This condition follows from the fact that the solution is a function of  $x_1$  alone and thus invariant for translations transverse to this direction, providing a convenient way to assign boundary conditions in the  $(x, y, z)$  system of coordinates. By choosing  $\tan \alpha = -r_1/r_2$  and  $\tan \beta = r_1/r_3$  together with  $\mathbf{s} = (n_x \Delta x, n_y \Delta y, n_z \Delta z)$ , one can show that the three shift integers  $n_x, n_y, n_z$  must obey

$$n_x - n_y \frac{r_1}{r_2} + n_z \frac{r_1}{r_3} = 0, \quad (40)$$

where  $\Delta x = \Delta y = \Delta z$  has been assumed and  $(r_1, r_2, r_3) = (1, 2, 4)$  will be used. The computational domain consists of  $[768 \times 8 \times 8]$  zones and spans  $(-0.75, 0.75)$  in the  $x$  direction while  $y, z \in [0, 0.015625]$ .

Table 3:  $L_1$  ( $\times 10^{-4}$ ) error for the 3D Shock Tube

	$\rho$	$V_1$	$V_2$	$V_3$	$B_1$	$B_2$	$B_3$	$p$
8W	3.0	2.0	4.8	4.7	<b>3.6</b>	4.5	5.1	5.0
CT	3.1	2.4	4.2	4.4	<b>0.5</b>	5.3	5.4	5.5
GLM	2.9	2.3	3.6	4.3	<b>0.5</b>	4.7	5.4	5.1
EGLM	3.5	2.5	4.3	4.8	<b>0.5</b>	5.3	5.9	7.3

In Fig. 5 we plot the primitive variable profiles for the GLM scheme at  $t = 0.02 \cos \alpha \cos \gamma$ . In accordance with the one dimensional solution (see also [10]), we observe the formation of a structure involving a contact discontinuity separating two fast shocks, two slow shocks and a pair of rotational discontinuities. The three-dimensional integration reproduces the correct behavior of all waves and the error in the longitudinal component of the field ( $B_1$  in Fig 5) exhibits small spurious oscillations about the same order of the CT scheme (see also, for instance, Fig. 7 in [16]).

A quantitative estimate of the error (using the one-dimensional  $L_1$  norm error) is obtained by comparing the three-dimensional results with a one-dimensional reference solution computed on 1024 zones until  $t = 0.02$ . The comparison, extended to the four selected integration schemes, is given in Table 3. We notice that the CT, GLM and EGLM schemes all yield errors of the same order of magnitude (typically  $10^{-4}$ ). Beware that these computations may be susceptible to small variations depending on implementation details (e.g. limiter, Courant number, etc.) and thus give a representative estimate of the error. For instance, the implementation of the CTU-CT scheme in the PLUTO code [20] is similar, although not exactly equivalent, to that of [16] who instead use piecewise parabolic reconstruction. Nevertheless, we have ascertained that the 8W scheme always performs the worst and the discrepancy becomes particular evident by looking at the longitudinal component of the field where the 8W scheme yields, once again, incorrect (although smaller than the previous 2D case) jumps. This is better illustrated in Fig. 6, where we compare the profiles of  $B_1$  for the four selected numerical schemes. We stress that, despite its non-conservative character, the EGLM formulation does not seem to produce incorrect jump conditions or wrong shock propagation speeds.

A resolution study, shown in the right panel of Fig 7, demonstrates that errors produced by the GLM and EGLM formulations are very much comparable and only weakly dependent on the  $\alpha$  parameter. Both schemes report a minimum at  $\alpha \approx 0.005 - 0.01$  regardless of the resolution, and the inferred order of convergence is approximately one as expected for solutions involving shock waves.

#### 4.4. Magnetic Field Loop Advection

This problem consists of a weak magnetic field loop being advected in a uniform velocity field. Since the total pressure is dominated by the thermal contribution, the magnetic field is essentially transported as passive scalar.

##### 4.4.1. Two-dimensional advection

Following [15, 14, 17], we employ a periodic computational box defined by  $x \in [-1, 1]$  and  $y \in [-0.5, 0.5]$  discretized on  $N_x \times N_x/2$  grid cells ( $N_x = 128$ ). Density and pressure are initially constant and equal to 1. The velocity of the flow is given by  $\mathbf{v} = (V_0 \cos \alpha, V_0 \sin \alpha, 1)$  with  $V_0 = \sqrt{5}$ ,  $\sin \alpha = 1/\sqrt{5}$  and  $\cos \alpha = 2/\sqrt{5}$ . The magnetic field is defined through its magnetic vector potential as

$$A_z = \begin{cases} A_0(R - r) & \text{if } r \leq R, \\ 0 & \text{if } r > R, \end{cases} \quad (41)$$

where  $A_0 = 10^{-3}$ ,  $R = 0.3$  and  $r = \sqrt{x^2 + y^2}$ . The simulations are allowed to evolve until  $t = 2$  ensuring the crossing of the loop twice through the periodic boundaries.

In Fig. 8 we show the magnetic energy density for the 8W, GLM and CT schemes using  $C_a = 0.8$  (top) and  $C_a = 0.4$  (bottom), along with the field lines shape. The circular shape of the loop is best preserved with the CT and GLM schemes while some distortions are visible using the 8 wave formulation. Using

$C_a = 0.4$  with the GLM scheme yields slightly better results, while the CT does not seem to be affected by the choice of the Courant number.

The time-history of the magnetic energy density (left panel in Fig 9) reveals that the numerical dissipation is essentially similar for all schemes, being smaller at larger Courant numbers. At the quantitative level, our results are similar and in good agreement with those of other investigators (e.g., [15, 14, 17]).

The ability of the GLM scheme in preserving the divergence-free condition is monitored by checking the growth of  $B_z$  in time: owing to a non-vanishing  $z$  component of velocity, in fact, we expect  $B_z$  to grow in time with a rate  $\propto v_z \nabla \cdot \mathbf{B}$  as seen from the induction equation. In the middle panel of Fig. 9 we plot the volume-averaged value of  $B_z$  as a function of time for  $N_x = 64, 128, 256$ . The nominal value is  $\sim 10^{-3}$  of the initial field strength, decreasing with resolution. Notice that the observed order of convergence is  $\sim 0.6 - 0.7$  and thus sub-linear as expected for a linearly degenerate wave in Godunov-type schemes, in accordance with the results of [5].

Computations carried with different values of  $\alpha$  reveal that divergence errors are minimized for  $\alpha \gtrsim 0.01$  while errors in  $B_z$  become smallest for  $\alpha \approx 0.01$  (right panel in Fig 9). Despite this may generate some ambiguities in prescribing an optimal  $\alpha$  value, however, we see that its choice does not significantly affect the error and thus constitutes a minor effect on the solution.

#### 4.5. Three-dimensional field loop advection

A three-dimensional extension can be obtained by rotating the previous 2D configuration around one axis using the coordinate transformation given by Eq. (35) with  $\alpha = 0$  and  $\gamma = \tan^{-1} 1/2$ , see [16]. Even though the loop is rotated only around one axis, the velocity profile  $(v_x, v_y, v_z) = (1, 1, 2)$  makes the test intrinsically three-dimensional. We consider the computational box  $-0.5 \leq x \leq 0.5$ ,  $-0.5 \leq y \leq 0.5$ ,  $-1.0 \leq z \leq 1.0$ , resolved on a  $N \times N \times 2N$  grid. Boundary conditions are periodic in all directions.

A three-dimensional rendering of the magnetic energy density is shown in Fig. 10 for the selected schemes while relevant quantities are plotted in the three panels of Fig 11. All schemes show a similar amount of numerical dissipation, in agreement with the results of [16].

As for the 2D case, it is useful to check the growth of the magnetic field component  $B_3 = (-B_x + 2B_z)/\sqrt{5}$  orthogonal to the original  $(x_1, x_2)$  plane where the loop is two-dimensional. Analytically, the magnetic field component in this direction is a trivial constant of motion since

$$\frac{\partial B_3}{\partial t} = v_3 \left( \frac{\partial B_1}{\partial x_1} + \frac{\partial B_2}{\partial x_2} \right) = 0. \quad (42)$$

The numerical integration in the rotated  $(x, y, z)$  Cartesian frame, however, preserves this condition only to some accuracy which strongly reflects the ability of the scheme in controlling the divergence-free constraint (this is true for all presented numerical methods). The middle panel in Fig 11 shows the volume-integrated value of  $|B_3|$ , normalized to the initial field strength  $B_0 = 10^{-3}$  for three different resolutions  $N = 32, 64, 128$ . Our results reveal that the value of  $B_3$  grows slowly in time while remaining reasonably small. The convergence rate ( $\approx 0.6 - 0.7$ ) is approximately the same as the one observed in the 2D case.

The dependency on  $\alpha$  is illustrated in the right panel Fig 11 showing that divergence errors are progressively reduced for  $\alpha \gtrsim 0.03$  although this has very little effect on the growth of  $B_3$ .

#### 4.6. Two-dimensional Rotor problem

The rotor problem consists of a dense disk rotating in a static medium threaded by an initially uniform magnetic field. As the rotor spins, the magnetic field gets wrapped around the disk creating torsional Alfvén waves, stemming from the rotating disk and moving towards the surrounding gas. This interaction slows down the disk by extracting angular momentum. On the other hand, the build-up of magnetic pressure around the rotor causes its compression.

Table 4: Parameter sets used for the first and second versions of the three-dimensional blast wave problem.

	$p_{\text{in}}$	$p_{\text{out}}$	$B_0$	$\theta$	$r_0$	$t_{\text{stop}}$
Test 1	$10^2$	1	10	$\pi/4$	0.125	0.02
Test 2	$10^4$	1	100	0	0.1	$2.5 \cdot 10^{-3}$

We initialized the problem on the Cartesian box  $x, y \in [-\frac{1}{2}, \frac{1}{2}]$  with outflow boundary conditions and use  $400^2$  grid points. The primitive variable profiles at the beginning of the simulation are given by

$$(\rho, v_x, v_y) = \begin{cases} (10, -\omega y, \omega x) & \text{if } r \leq r_0, \\ \left(1 + 9f, -f\omega y \frac{r_0}{r}, f\omega x \frac{r_0}{r}\right) & \text{if } r_0 < r < r_1, \\ (1, 0, 0) & \text{if } r \geq r_1, \end{cases} \quad (43)$$

where  $\omega = 20$ ,  $r_0 = 0.1$ ,  $r_1 = 0.115$ ,  $r = \sqrt{x^2 + y^2}$  and the taper function is  $f = (r_1 - r)/(r_1 - r_0)$ . Thermal pressure is initially uniform and equal to one ( $\Gamma = 1.4$  is used). The magnetic field has only one non-vanishing component,  $B_x = 5/\sqrt{4\pi}$ .

The maps of density, magnetic energy and sonic Mach number are displayed in Fig. 12 at  $t = 0.15$  for the GLM and the CT schemes, when the torsional Alfvén waves have almost reached the outer boundaries. The strength of the scheme is also measured by its ability to preserve the circular shape of the sonic Mach number profile in the central region, an essential feature of the solution, [17]. This is better shown in Fig. 13 where an enlargement of the central region reveals that the GLM and CT schemes have developed extremely similar Mach number contours and the absence of spurious peaks (that would be caused by pressure undershoots) advocates towards the validity of the scheme.

#### 4.7. Three Dimensional Blast Wave

The MHD blast wave problem has been specifically designed to show the scheme ability to handle strong shock waves propagating in highly magnetized environments, see for instance [28, 2, 29, 16, 17]. Depending on the strength of the magnetic field, it can become a rather arduous test leading to unphysical densities or pressures if the divergence-free condition is not properly controlled and the scheme does not introduce adequate dissipation across oblique discontinuous features. Here, we consider a three-dimensional configuration on the unit cube  $[-1/2, 1/2]^3$  discretized on  $200^3$  computational zones. The medium is initially at rest ( $\mathbf{v} = \mathbf{0}$ ) and threaded by a constant uniform magnetic field lying in the  $xz$  plane and forming an angle  $\theta$  with the vertical  $z$  direction,  $\mathbf{B} = B_0 (\sin \theta \hat{x} + \cos \theta \hat{z})$ . A spherical region of high thermal pressure is initialized,

$$p = \begin{cases} p_{\text{in}} & \text{for } \sqrt{x^2 + y^2 + z^2} < r_0, \\ p_{\text{out}} & \text{otherwise.} \end{cases} \quad (44)$$

We consider two different versions of the same test problem with parameters given in Table 4. In the first one, taken from [16], the field forms an angle  $\theta = \pi/4$  with the  $z$  axis and the largest magnetization achieved outside the sphere is  $\beta = 2p_{\text{out}}/B^2 = 2 \cdot 10^{-2}$ . In the second version, we follow [29] and adopt a larger field strength (with  $\theta = 0$ ) yielding a more severe configuration with  $\beta = 2 \cdot 10^{-4}$ .

The over-pressurized spherical region sets a blast wave delimited by an outer fast forward shock propagating (nearly) radially, see Fig 14 and 16. Magnetic field lines pile up behind the shock in the direction transverse to the initial field orientation ( $\theta = \pi/4$  and  $\theta = 0$  for the two cases) thus building a region of higher magnetic pressure. In these regions the shock becomes magnetically dominated and only weakly compressive ( $\delta\rho/\rho \sim 1.2$  in both cases). The inner structure is delimited by an oval-shaped slow shock adjacent to a contact discontinuity and the two fronts tend to blend together as the propagation becomes perpendicular to the field lines. The magnetic energy increases behind the fast shock and decreases downstream of the slow shock. The resulting explosion becomes highly anisotropic and magnetically confined.

Computed results for the first configuration are shown in Fig 14, where we display linearly scaled maps of gas pressure, magnetic and kinetic energy densities for the GLM scheme (top), EGLM (middle) and CT schemes (bottom). The computations are in excellent agreement and no noticeable difference can be discerned from the images. Moreover, our results favorably compare to those of [16]. To further ascertain the validity of the non-conservative EGLM scheme, we plot, in Fig 15, one-dimensional slices (along the  $x$  direction in the  $yz$  mid-plane) showing the density and pressure obtained with the EGLM and CT integrations.

Computations for the second configuration could be obtained only with the EGLM scheme, since the CT scheme failed even with a minmod limiter ( $\beta = 1$  in Eq. 18). In Fig. 16 we plot contour levels for density, pressure, velocity and magnetic energy. These results comply with those of [29] who used a CT scheme together with a Runge-Kutta time stepping and an HLL Riemann solver. They also share similarities with the 2D strong field case discussed in [17] who used a different implementation of the CT scheme. Partially owing also to the increased resolution ( $200^3$  instead of  $144^3$ ) our CTU-EGLM algorithm shows considerably reduced numerical diffusion while being robust in keeping sharp profiles of the discontinuities.

## 5. Conclusions

A second-order, cell-centered numerical scheme for the solution of the MHD equations in two and three dimensions has been proposed. Fully unsplit integration resorts to the Corner Transport Method of Colella [8] and the divergence-free condition is controlled by using a constrained formulation of the MHD equations where the induction equation is coupled to a generalized Lagrange multiplier (GLM, [12]). The system is hyperbolic, easy to implement and does not require expensive cleaning projection steps associated with the solution of elliptic problems. The GLM scheme is fully conservative in mass, momentum, energy and magnetic induction, although we have also considered a slightly modified variant (EGLM) which infringes momentum and energy conservation.

In order to assess the reliability and accuracy of the schemes we have performed a number of code benchmarks on standard two- and three-dimensional MHD test problems. Results have been compared with two different numerical schemes: a non-conservative cell-centered method based on the 8-wave formulation (8W, [22]) and the constrained transport (CT) method where the magnetic field has a staggered collocation. Both the GLM and EGLM schemes give excellent results in terms of accuracy and robustness and do not show, in the tests presented here, any evidence for incorrect jump conditions or wrong wave propagation, as found for the eight wave formulation (in agreement with Tóth [26]). This has been verified on problems involving discontinuous waves and holds true for both the conservative GLM formulation *and* the EGLM variant which breaks momentum and energy conservation. In this perspective, our results seem to indicate that the presence of source terms in the equations does not necessarily lead to erroneous jumps. Instead, we have found the non-conservative formulation to be more robust for problems involving the propagation of oblique strongly magnetized shocks. Although, this behavior may be attributed to discretization, such a study is beyond the scope of the present paper. The comparison has also revealed an excellent quantitative agreement with the CTU-CT scheme (in the version of [15, 16]) showing errors with comparable magnitude and similar order of convergence while retaining the desired robustness and stability.

For these reasons, we believe that the proposed CTU-GLM and CTU-EGLM schemes provide excellent competitive alternatives to modern staggered-mesh algorithms while being considerably easier and more flexible in their implementations. Owing to the cell-centered collocation of all of the flow fields, the CTU-GLM scheme can be easily generalized to resistive MHD, adaptive and/or unstructured grids and to higher than second-order spatially-accurate numerical schemes. Some of these issues will be presented in forthcoming papers.

### A. Characteristic Decomposition of the GLM-MHD Equations

The  $9 \times 9$  matrix  $A_x$  of the primitive MHD equations introduced in §3.1.1 can be decomposed as  $A_x = R\Lambda L$  where  $\Lambda = \text{diag}(\lambda^k)$  contains the eigenvalues (see Eq. 14) while the rows of  $L$  and columns of  $R$  are the

corresponding left and right eigenvectors of  $\mathbf{A}_x$ , respectively. Adopting the scaling of [22] we define

$$\alpha_f^2 = \frac{\alpha^2 - c_s^2}{c_f^2 - c_s^2}, \quad \alpha_s^2 = \frac{c_f^2 - \alpha^2}{c_f^2 - c_s^2} \quad (45)$$

and

$$\beta_y = \frac{B_y}{\sqrt{B_y^2 + B_z^2}}, \quad \beta_z = \frac{B_z}{\sqrt{B_y^2 + B_z^2}} \quad (46)$$

where  $\alpha = \sqrt{\Gamma p / \rho}$  denotes the speed of sound. With this notation, the right eigenvectors in matrix form will be given by

$$\mathbf{R} = \begin{pmatrix} 0 & \rho\alpha_f & 0 & \rho\alpha_s & 1 & \rho\alpha_s & 0 & \rho\alpha_f & 0 \\ 0 & -c_f\alpha_f & 0 & -\alpha_s c_s & 0 & \alpha_s c_s & 0 & c_f\alpha_f & 0 \\ 0 & \alpha_s c_s \beta_y S & -\frac{\beta_z}{\sqrt{2}} & -\alpha_f c_f \beta_y S & 0 & \alpha_f c_f \beta_y S & -\frac{\beta_z}{\sqrt{2}} & -\alpha_s c_s \beta_y S & 0 \\ 0 & \alpha_s c_s \beta_z S & \frac{\beta_y}{\sqrt{2}} & -\alpha_f c_f \beta_z S & 0 & \alpha_f c_f \beta_z S & \frac{\beta_y}{\sqrt{2}} & -\alpha_s c_s \beta_z S & 0 \\ 1 & 0 & 0 & 0 & 0 & 0 & 0 & 0 & 1 \\ 0 & \alpha_s \sqrt{\rho}\alpha\beta_y & -\sqrt{\frac{\rho}{2}}\beta_z & -\alpha_f \sqrt{\rho}\alpha\beta_y & 0 & -\alpha_f \sqrt{\rho}\alpha\beta_y & \sqrt{\frac{\rho}{2}}\beta_z & \alpha_s \sqrt{\rho}\alpha\beta_y & 0 \\ 0 & \alpha_s \sqrt{\rho}\alpha\beta_z & \sqrt{\frac{\rho}{2}}\beta_y & -\alpha_f \sqrt{\rho}\alpha\beta_z & 0 & -\alpha_f \sqrt{\rho}\alpha\beta_z & -\sqrt{\frac{\rho}{2}}\beta_y & \alpha_s \sqrt{\rho}\alpha\beta_z & 0 \\ 0 & \alpha_f \Gamma p & 0 & \alpha_s \Gamma p & 0 & \alpha_s \Gamma p & 0 & \alpha_f \Gamma p & 0 \\ -c_h & 0 & 0 & 0 & 0 & 0 & 0 & 0 & c_h \end{pmatrix} \quad (47)$$

where  $S = \text{sign}(B_x)$ . On the other hand, the left eigenvectors are

$$\mathbf{L} = \begin{pmatrix} 0 & 0 & 0 & 0 & \frac{1}{2} & 0 & 0 & 0 & -\frac{1}{2c_h} \\ 0 & -\frac{\alpha_f c_f}{2\alpha^2} & \frac{\alpha_s c_s \beta_y S}{2\alpha^2} & \frac{\alpha_s c_s \beta_z S}{2\alpha^2} & 0 & \frac{\alpha_s \beta_y}{2\sqrt{\rho}\alpha} & \frac{\alpha_s \beta_z}{2\sqrt{\rho}\alpha} & \frac{\alpha_f}{2\rho\alpha^2} & 0 \\ 0 & 0 & -\frac{\beta_z}{\sqrt{2}} & \frac{\beta_y}{\sqrt{2}} & 0 & -\frac{\beta_z}{\sqrt{2}\rho} & \frac{\beta_y}{\sqrt{2}\rho} & 0 & 0 \\ 0 & -\frac{\alpha_s c_s}{2\alpha^2} & -\frac{\alpha_f c_f \beta_y S}{2\alpha^2} & -\frac{\alpha_f c_f \beta_z S}{2\alpha^2} & 0 & -\frac{\alpha_f \beta_y}{2\sqrt{\rho}\alpha} & -\frac{\alpha_f \beta_z}{2\sqrt{\rho}\alpha} & \frac{\alpha_s}{2\rho\alpha^2} & 0 \\ 1 & 0 & 0 & 0 & 0 & 0 & 0 & 0 & -\frac{1}{\alpha^2} \\ 0 & \frac{\alpha_s c_s}{2\alpha^2} & \frac{\alpha_f c_f \beta_y S}{2\alpha^2} & \frac{\alpha_f c_f \beta_z S}{2\alpha^2} & 0 & -\frac{\alpha_f \beta_y}{2\sqrt{\rho}\alpha} & -\frac{\alpha_f \beta_z}{2\sqrt{\rho}\alpha} & \frac{\alpha_s}{2\rho\alpha^2} & 0 \\ 0 & 0 & -\frac{\beta_z}{\sqrt{2}} & \frac{\beta_y}{\sqrt{2}} & 0 & \frac{\beta_z}{\sqrt{2}\rho} & -\frac{\beta_y}{\sqrt{2}\rho} & 0 & 0 \\ 0 & \frac{\alpha_f c_f}{2\alpha^2} & -\frac{\alpha_s c_s \beta_y S}{2\alpha^2} & -\frac{\alpha_s c_s \beta_z S}{2\alpha^2} & 0 & \frac{\alpha_s \beta_y}{2\sqrt{\rho}\alpha} & \frac{\alpha_s \beta_z}{2\sqrt{\rho}\alpha} & \frac{\alpha_f}{2\rho\alpha^2} & 0 \\ 0 & 0 & 0 & 0 & \frac{1}{2} & 0 & 0 & 0 & \frac{1}{2c_h} \end{pmatrix}. \quad (48)$$

## References

- [1] A. Artebrant, M. Torrilhon, Increasing the accuracy in locally divergence-preserving finite-volume schemes for MHD, *J. Comput. Phys.* 227 (2008) 3405-3427
- [2] D.S. Balsara, D.S. Spicer, A Staggered Mesh Algorithm Using High Order Godunov Fluxes to Ensure Solenoidal Magnetic Fields in Magnetohydrodynamics Simulations, *J. Comput. Phys.* 149 (1999) 270
- [3] D.S. Balsara, Second-order-accurate schemes for magnetohydrodynamics with divergence-free reconstruction, *Astrophysical Journal Supplement*, 151 (2004), 149
- [4] D.S. Balsara, J. Kim, A comparison between divergence-cleaning and staggered-mesh formulations for numerical magnetohydrodynamics, *ApJ* 602 (2004) 1079.

- [5] J.W. Banks, T. Aslam, W.J. Rider, On sub-linear convergence for linearly degenerate waves in capturing schemes, *J. Comput. Phys.* 227 (2008) 6985-7002.
- [6] J. U. Brackbill and D. C. Barnes, The effect of nonzero  $\nabla \cdot \mathbf{B}$  on the numerical solution of the magnetohydrodynamics equations, *J. Comput. Phys.* 35, 426 (1980).
- [7] P. Cargo, G. Gallice, Roe Matrices for Ideal MHD and Systematic Construction of Roe Matrices for Systems of Conservation Laws, *J. Comput. Phys.* 136 (1997) 446.
- [8] P. Colella, Multidimensional upwind methods for hyperbolic conservation laws, *J. Comput. Phys.* 87 (1990) 171.
- [9] R.K. Crockett, P. Colella, R.T. Fisher, R.I. Klein, C.F. McKee, An Unsplit, cell-centered Godunov method for ideal MHD, *J. Comput. Phys.* 203 (2005) 422.
- [10] W. Dai, P.R. Woodward, An Approximate Riemann Solver for Ideal Magnetohydrodynamics *J. Comput. Phys.* 111 (1994) 372
- [11] W. Dai, P.R. Woodward, A Simple Finite Difference Scheme for Multidimensional Magnetohydrodynamical Equations, *J. Comput. Phys.* 142 (1998) 331
- [12] A. Dedner, F. Kemm, D. Kröner, C.D. Munz, T. Schnitzer, M. Wesenberg, Hyperbolic divergence cleaning for the MHD equations, *J. Comput. Phys.* 175 (2002) 645-673.
- [13] C.R. Evans, J.F. Hawley, Simulation of magnetohydrodynamics flows - A constrained transport method, *ApJ* 332 (1988) 659
- [14] S. Fromang, P. Hennebelle, R. Teyssier, A high order Godunov scheme with constrained transport and adaptive mesh refinement for astrophysical magnetohydrodynamics. *Astronomy & Astrophysics* 457 (2006) 371.
- [15] T. Gardiner, J. Stone, An unsplit Godunov method for ideal MHD via constrained transport, *J. Comput. Phys.* 205 (2005) 509.
- [16] T. Gardiner, J. Stone, An unsplit Godunov method for ideal MHD via constrained transport in three dimensions, *J. Comput. Phys.* 227 (2008) 4123.
- [17] D. Lee, A.E. Deane, An unsplit staggered mesh scheme for multidimensional magnetohydrodynamics, *J. Comput. Phys.* 228 (2009) 952.
- [18] P. Londrillo, L. Del Zanna, On the divergence-free condition in Godunov-type schemes for ideal magnetohydrodynamics: the upwind constrained transport method, *J. Comput. Phys.* 195 (2004) 17
- [19] S. Massaglia, G. Bodo, A. Mignone, P. Rossi, *Jets From Young Stars III: Numerical MHD and Instabilities*, Lecture Notes in Physics, Volume 754. ISBN 978-3-540-76966-8. Springer-Verlag Berlin Heidelberg, 2008
- [20] A. Mignone, Bodo G., Massaglia S. et al., PLUTO: A Numerical Code for Computational Astrophysics, *ApJS* 170 (2007) 228
- [21] K. G. Powell, An Approximate Riemann Solver for Magnetohydrodynamics (That Works in More than One Dimension), ICASE-Report 94-24 (NASA CR-194902) (NASA Langley Research Center, Hampton, VA 23681-0001, 8. April 1994).
- [22] K. G. Powell, P. L. Roe, T. J. Linde, T. I. Gombosi, and D. L. De Zeeuw, A solution-adaptive upwind scheme for ideal magnetohydrodynamics, *J. Comput. Phys.* 154, 284 (1999).
- [23] J.A. Rossmannith, An Unstaggered, High-Resolution Constrained Transport Method for Magnetohydrodynamic Flows, *SIAM J. Sci. Comput.* 28 (2006), 1766-1797
- [24] D. Ryu, T.W. Jones, A. Frank, Numerical Magnetohydrodynamics in Astrophysics: Algorithm and Tests for multidimensional flows, *ApJ* 452 (1995) 785
- [25] D. Ryu, F. Miniati, T.W. Jones, A. Frank A divergence-free upwind code for multidimensional magnetohydrodynamic flows, *ApJ* 509 (1998) 244
- [26] G. Tóth, The  $\nabla \cdot \mathbf{B} = 0$  constraint in shock-capturing magnetohydrodynamics codes, *J. Comput. Phys.* 161 (2000) 605
- [27] M. Torrilhon, Locally Divergence-Preserving Upwind Finite Volume Schemes for Magnetohydrodynamics Equations, *Siam J. Sci. Comput.* 26 (2005) 1166
- [28] A.L. Zachary, A. Malagoli, P. Colella, A high-order Godunov method for multidimensional ideal MHD, *SIAM J. Sci. Comput.*, 15 (1994) 263
- [29] U. Ziegler, A central-constrained transport scheme for ideal magnetohydrodynamics, *J. Comput. Phys.* 196 (2004) 393

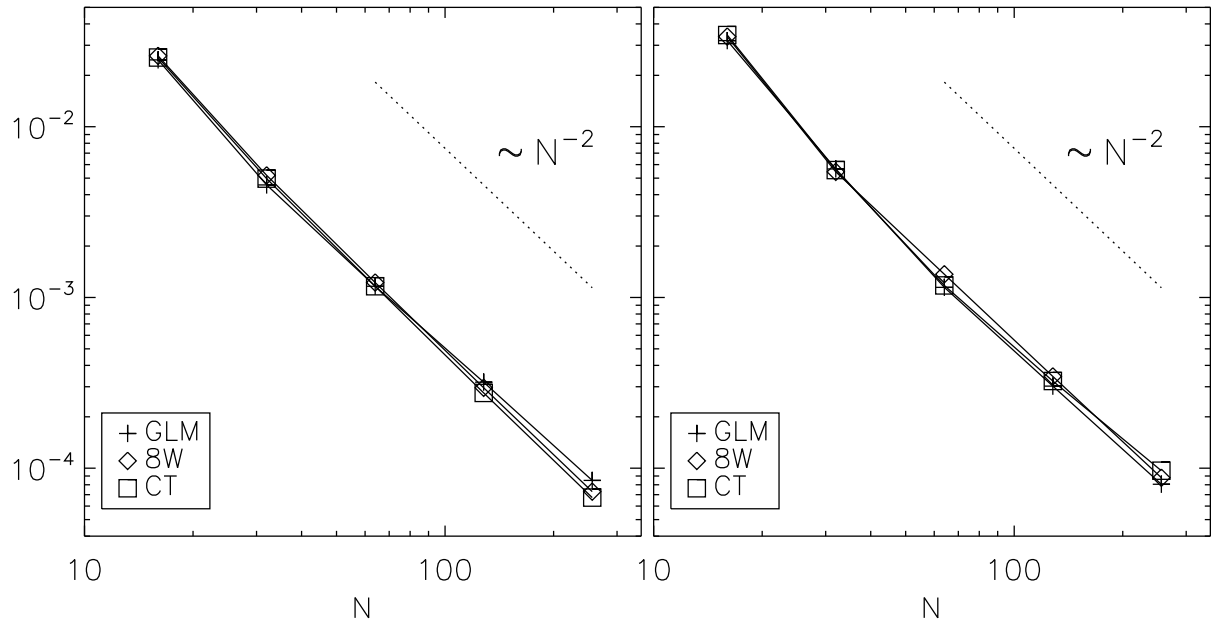


Figure 1:  $L_1$  norm errors for the 2D (left) and 3D (right) circularly polarized Alfvén wave test problem. Each symbol refers to results obtained with the GLM (plus sign), CT (square) and Powell's eight wave (rhombus) methods, while the dotted line gives the ideal second-order convergence slope. The Courant number  $C_a = 0.8$  and the final time step is  $1/\sqrt{5}$  (left) and  $1/3$  right.

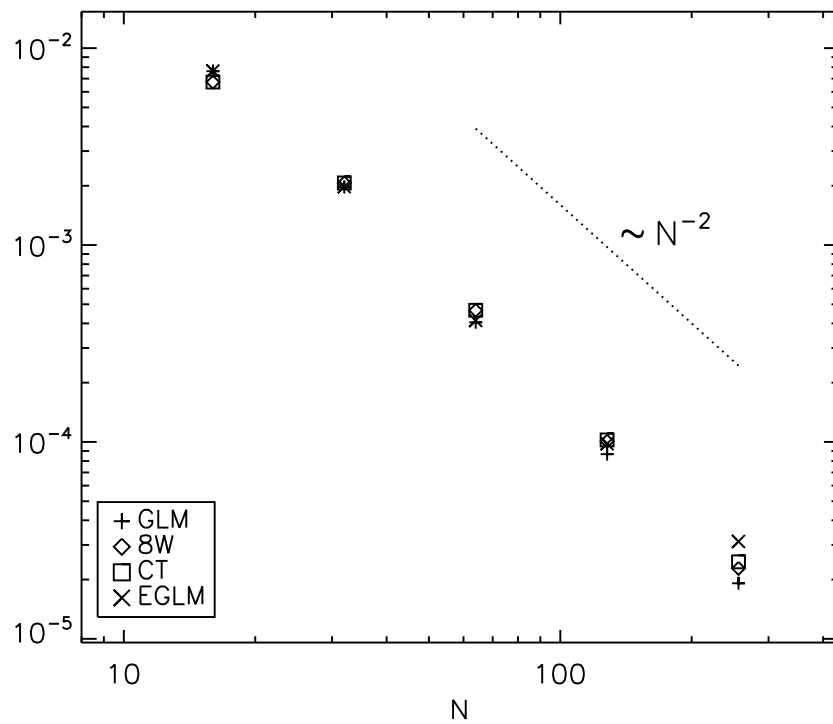


Figure 2:  $L_1$  norm errors for the non-linear, smooth flow test problem at  $t = 0.2$ . The different symbols refer to computations carried out with the GLM (plus signs), EGLM (ex signs), CT (squares) and Powell's eight wave method (rhombus) with Courant number  $C_a = 0.8$ . The dotted line gives the ideal second-order convergence slope.

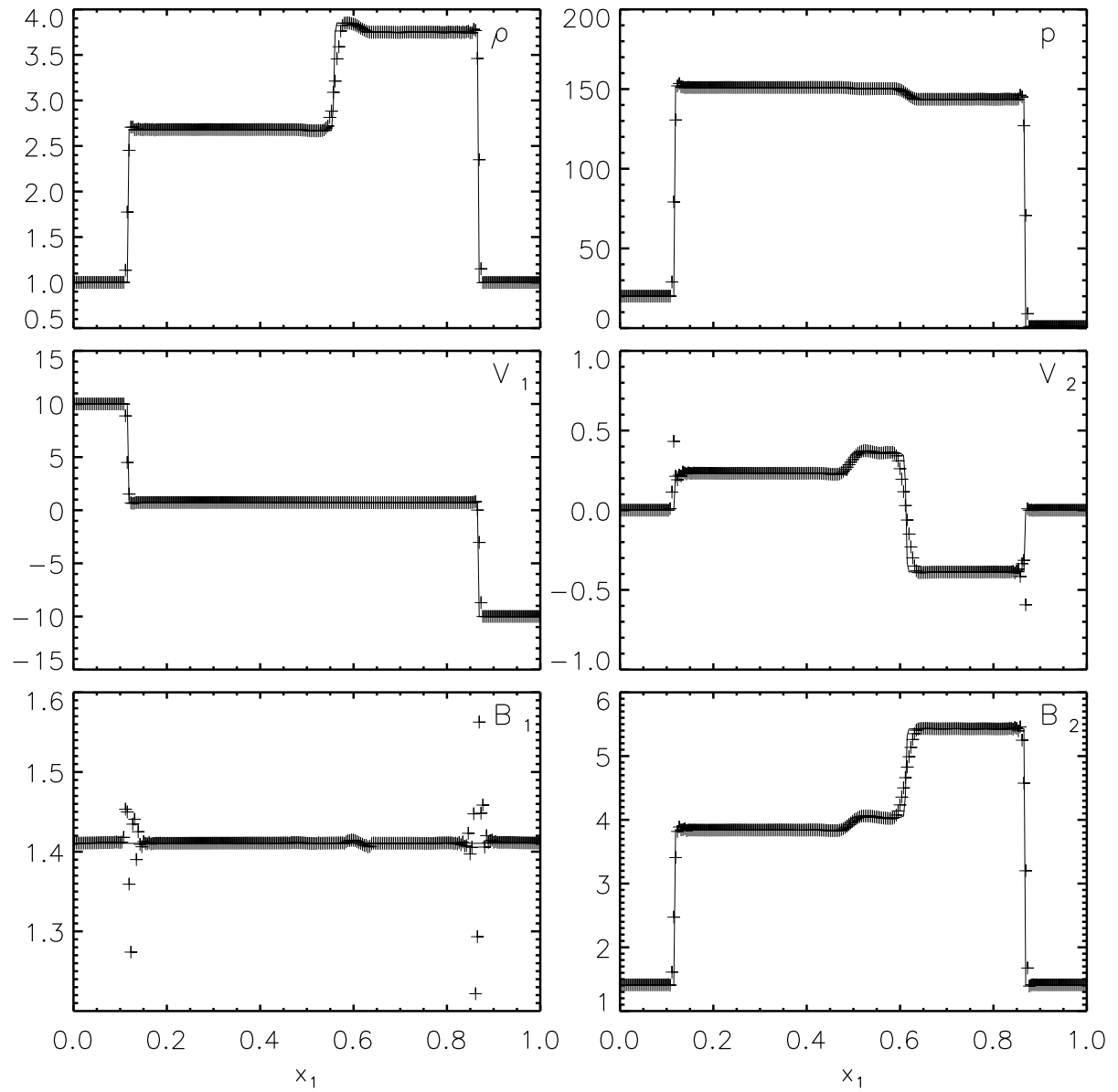


Figure 3: Primitive variable profiles for the 2D shock tube problem at  $t = 0.08 \cos \alpha$ , along the rotated direction  $x_1$ . The symbols correspond to the CTU-GLM solution whereas the solid lines represent the reference solution. From top to bottom and left to right, density, thermal pressure, velocity components and magnetic field components (parallel and perpendicular with respect to the  $x_1$  direction) are displayed.

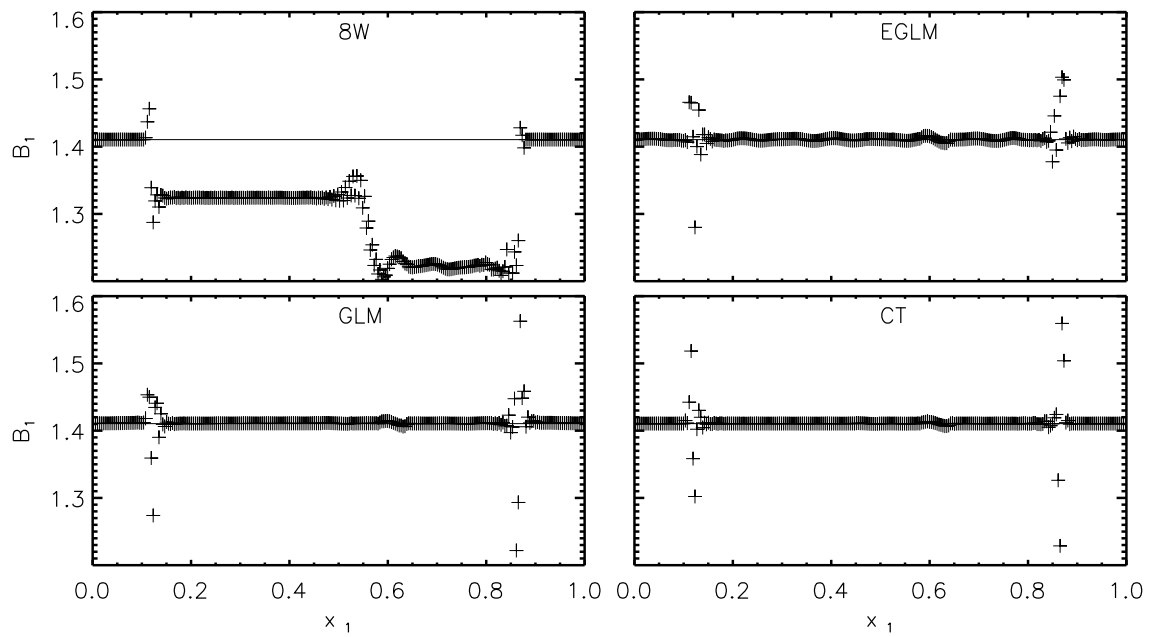


Figure 4: The parallel magnetic field component for the four schemes. Concordantly with the results of [26] the 8 wave formalism fails to capture the correct jumps. This problem is absent in the results of the other schemes and the field component remains close to the expected value  $5/\sqrt{4\pi}$  away from discontinuities. Spikes are found in proximity of shock waves and are of the same order of magnitude for GLM, EGLM and CT schemes.

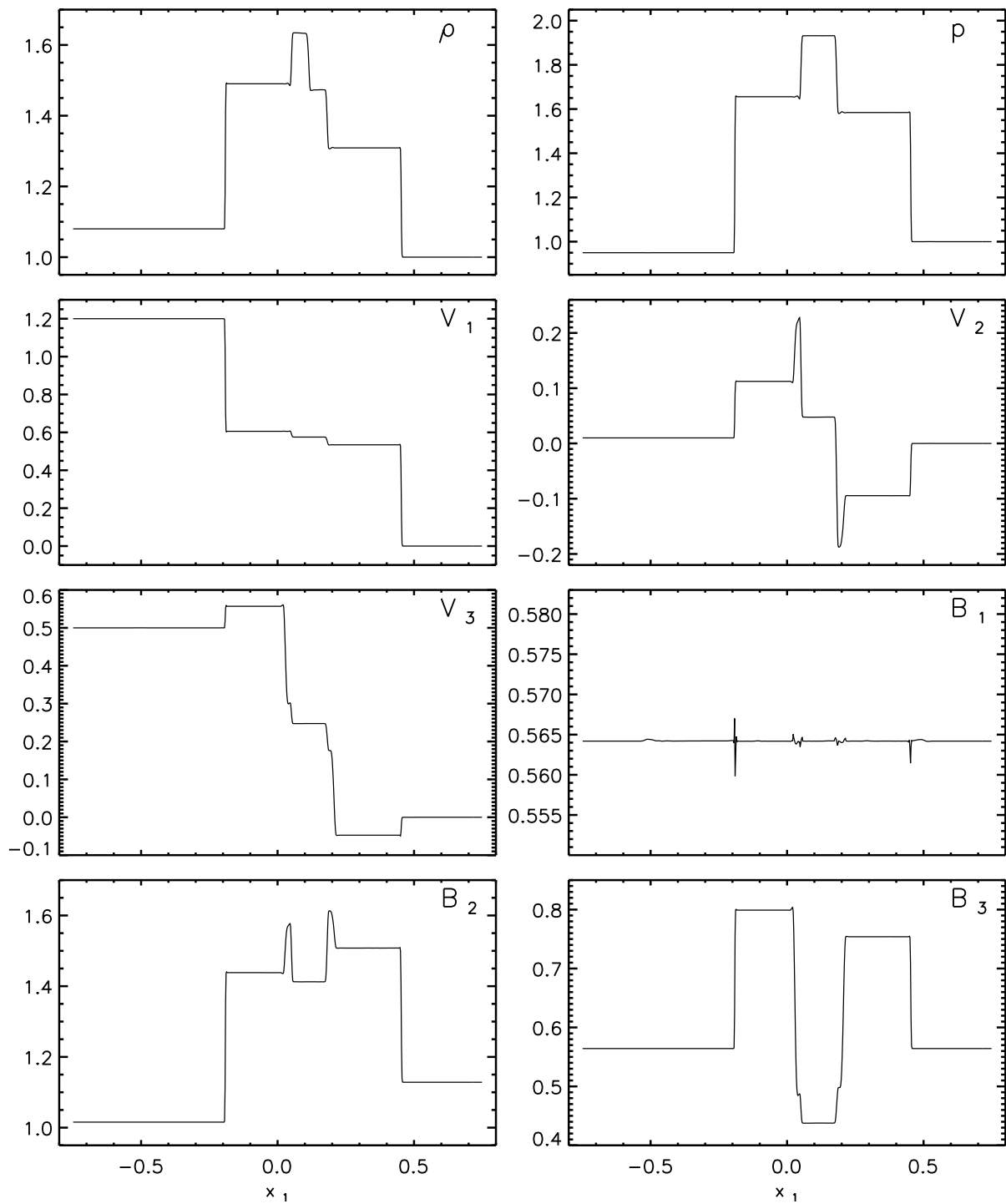


Figure 5: Primitive variable profiles for the 3D shock tube problem at  $t = 0.02 \cos \alpha \cos \gamma$ , along the rotated direction  $x_1$  .

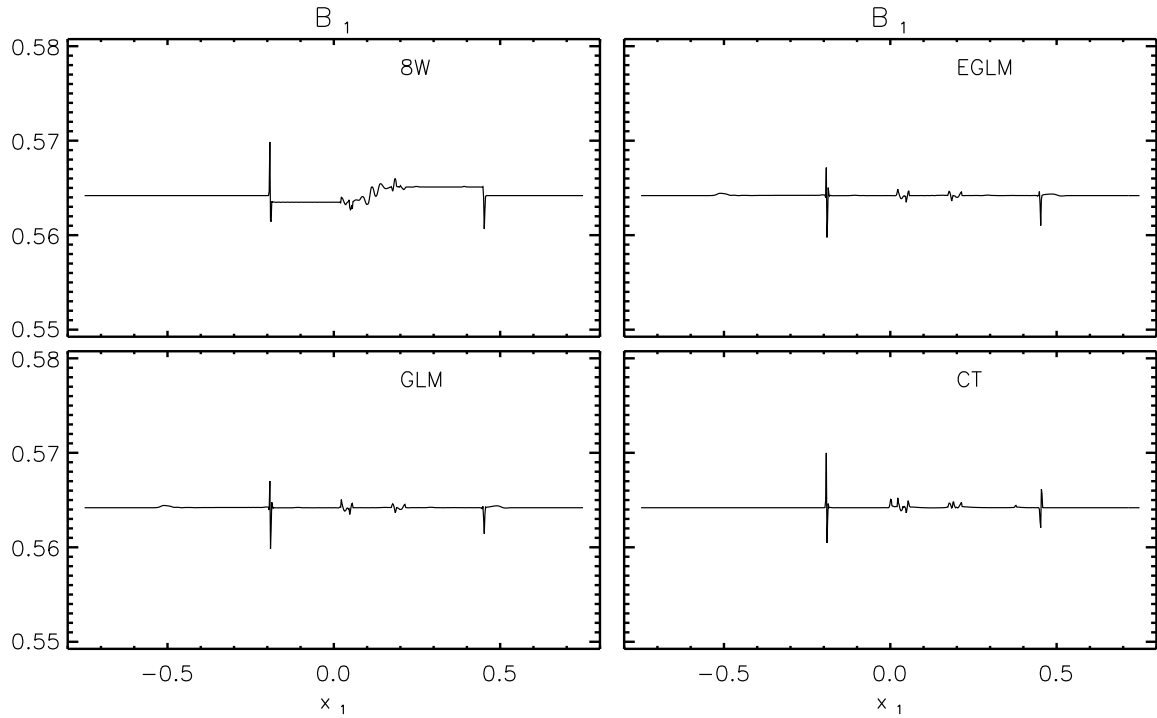


Figure 6: Comparison of the parallel component of the magnetic field for the 3D shock tube test. As in the 2D case, the error is minimal for all schemes with the exception of the 8-wave formalism. The latter fails to capture correctly the jump but the error is less prominent than the 2D case.

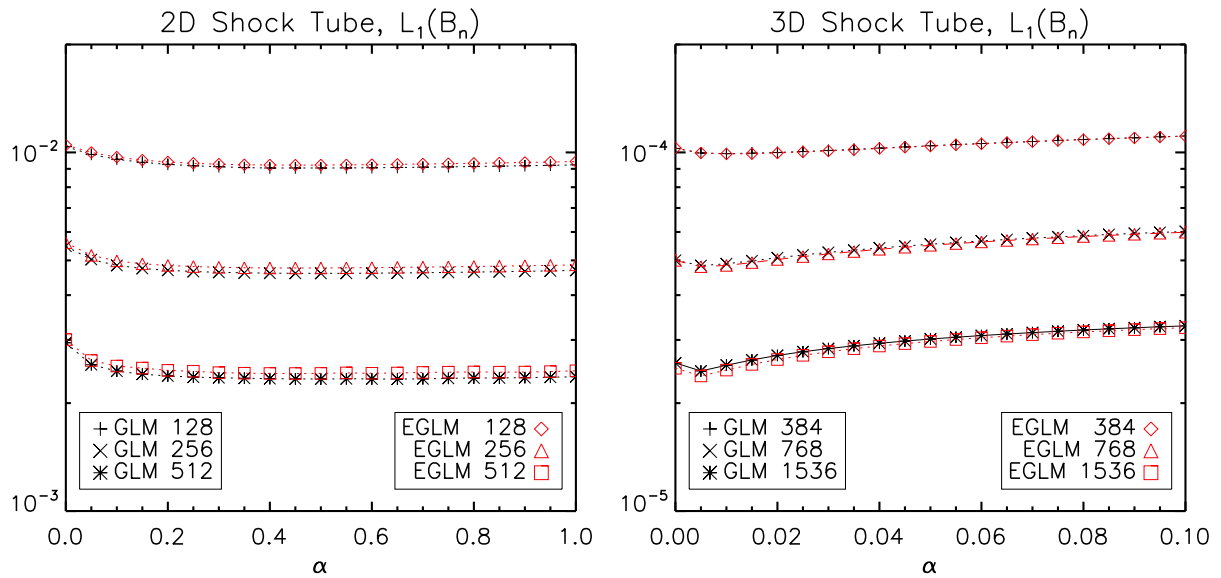


Figure 7:  $L_1$  norm errors of  $B_1$  (the magnetic field component in the direction orthogonal to the initial discontinuity) as functions of  $\alpha = \Delta hc_n / c_p^2$  for the 2D (left) and 3D (right) shock tube problem. The different symbols correspond to computations carried at different mesh resolutions:  $N_x = 128, 256, 512$  (in 2D) and  $N_x = 384, 768, 1536$  in 3D. Black and red symbols refer to results obtained with the GLM and EGLM formulations, respectively. The Courant numbers were 0.8 and 0.4 for 2 and 3D computations, respectively.

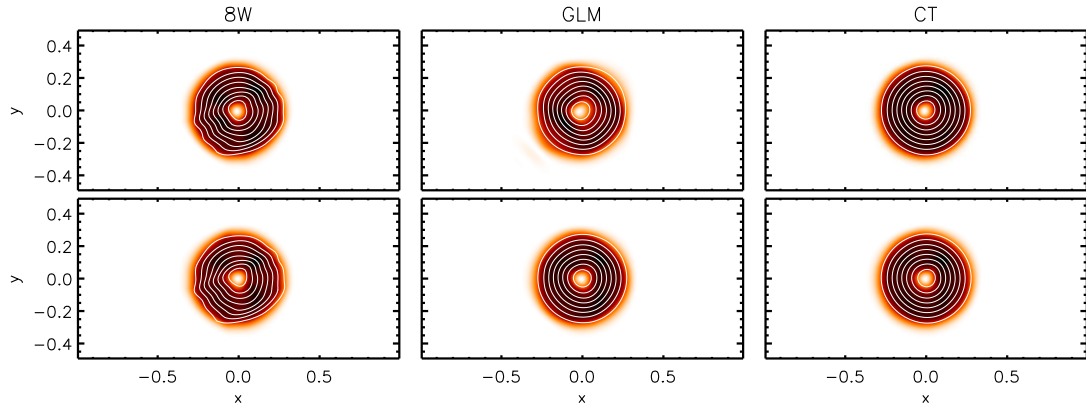


Figure 8: From left to right: magnetic energy density for the 2D field loop problem at  $t = 2$  for the 8W, GLM and CT schemes. Results have been computed with CFL numbers of 0.8 (top) and 0.4 (bottom). Overplotted are 9 isocontours of  $A_z$ , between  $10^{-5}$  and  $10^{-3}$ .

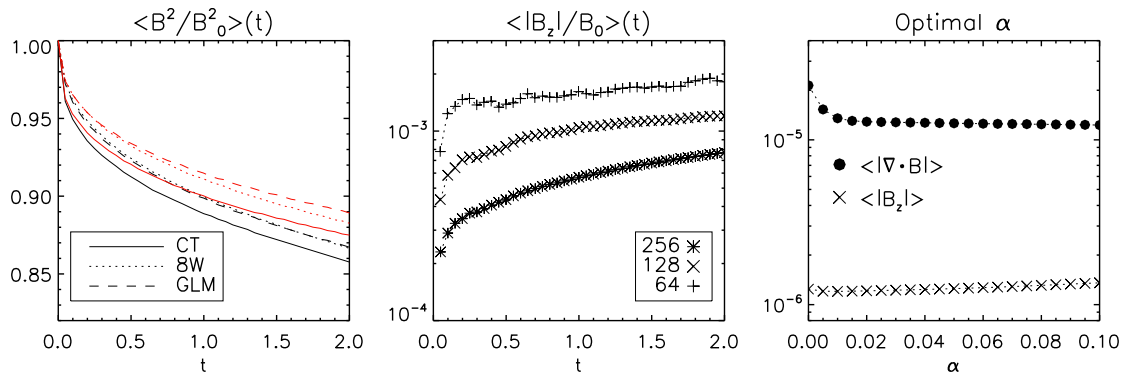


Figure 9: Leftmost panel: time evolution of the volume-integrated magnetic energy density (normalized to its initial value) for the 2D field loop advection problem. The black and red lines correspond, respectively, to computations carried with  $C_a = 0.4$  and  $C_a = 0.8$ . Middle panel: volume-averaged value of  $|B_z|$  (normalized to the initial value  $B_0 = 10^{-3}$ ) as a function of time for three different grid resolutions (256, 128 and 64 corresponding to stars, "x" and plus signs). Rightmost panel: volume-averaged values of  $|\nabla \cdot \mathbf{B}|$  and  $|B_z|$  for different values of the  $\alpha$  parameter controlling monopole damping at the resolution  $N_x = 128$  points.

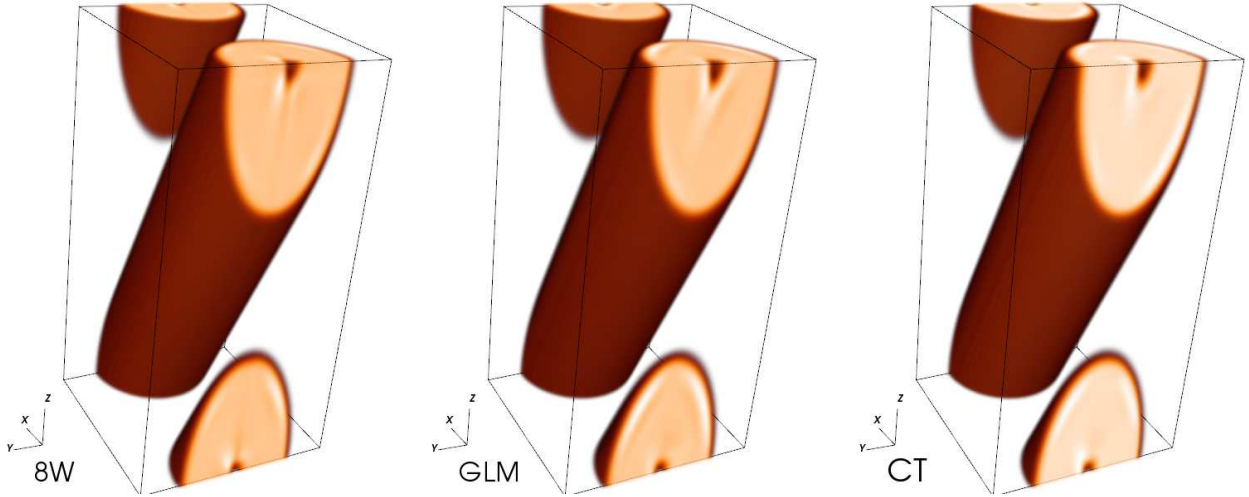


Figure 10: Magnetic energy density for the 3D field loop problem at  $t = 1$  at the resolution of  $128 \times 128 \times 256$ . From left to right: results obtained with the 8W, GLM and CT schemes.

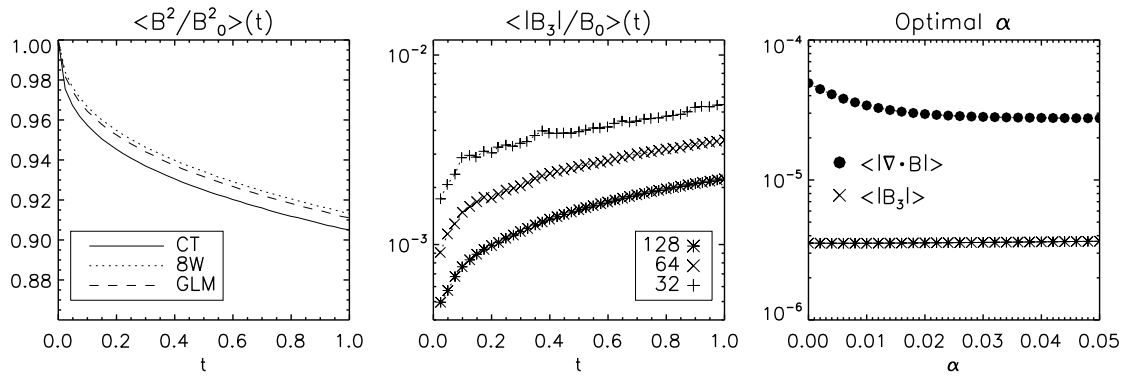


Figure 11: Same as Fig 9 for the 3D field loop advection test. From left to right: time history of the (normalized) volume-integrated magnetic field energy, (normalized) average value of  $|B_3|$  (magnetic field component orthogonal to the original 2D plane) and volume averages of  $|\nabla \cdot \mathbf{B}|$  and  $|B_3|$  as functions of the  $\alpha$  parameter.

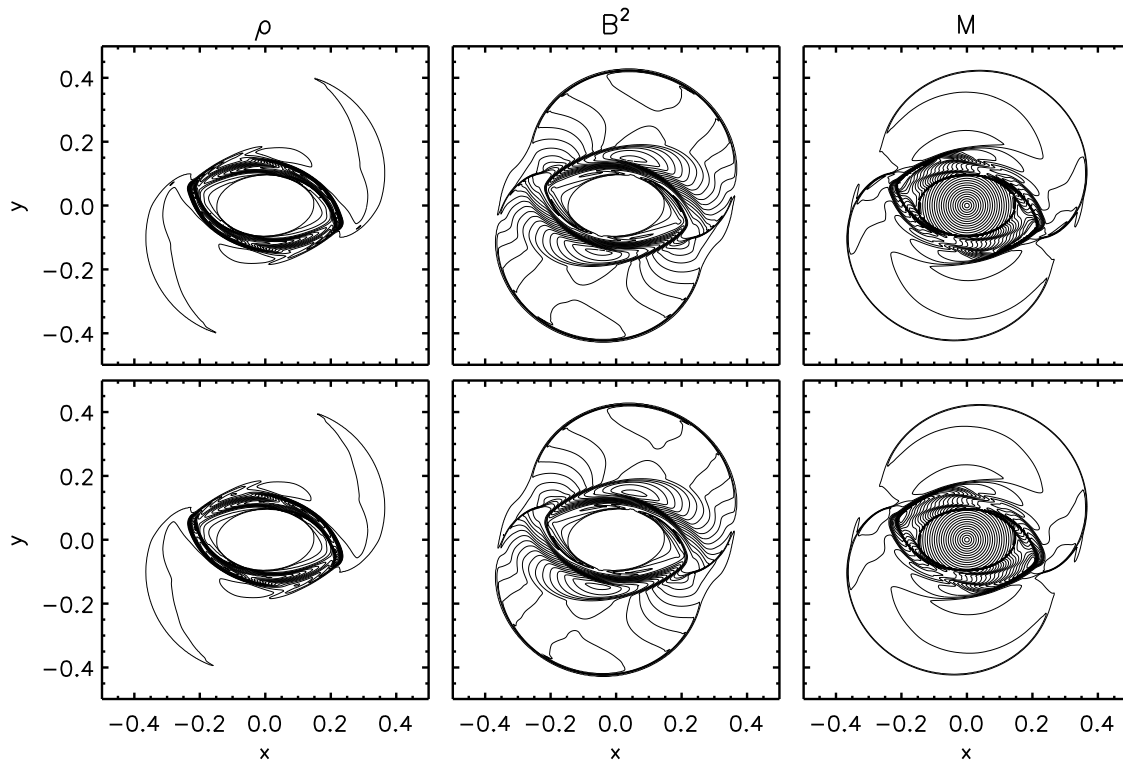


Figure 12: Density, magnetic energy and sonic Mach number for the rotor problem at  $t = 0.15$  obtained with the GLM (upper panels) and the CT (lower panels) methods. 20 levels are displayed, the range of which is  $0.5 \leq \rho \leq 13$ ,  $0.04 \leq B^2 \leq 5.2$  and  $0 \leq M \leq 4$

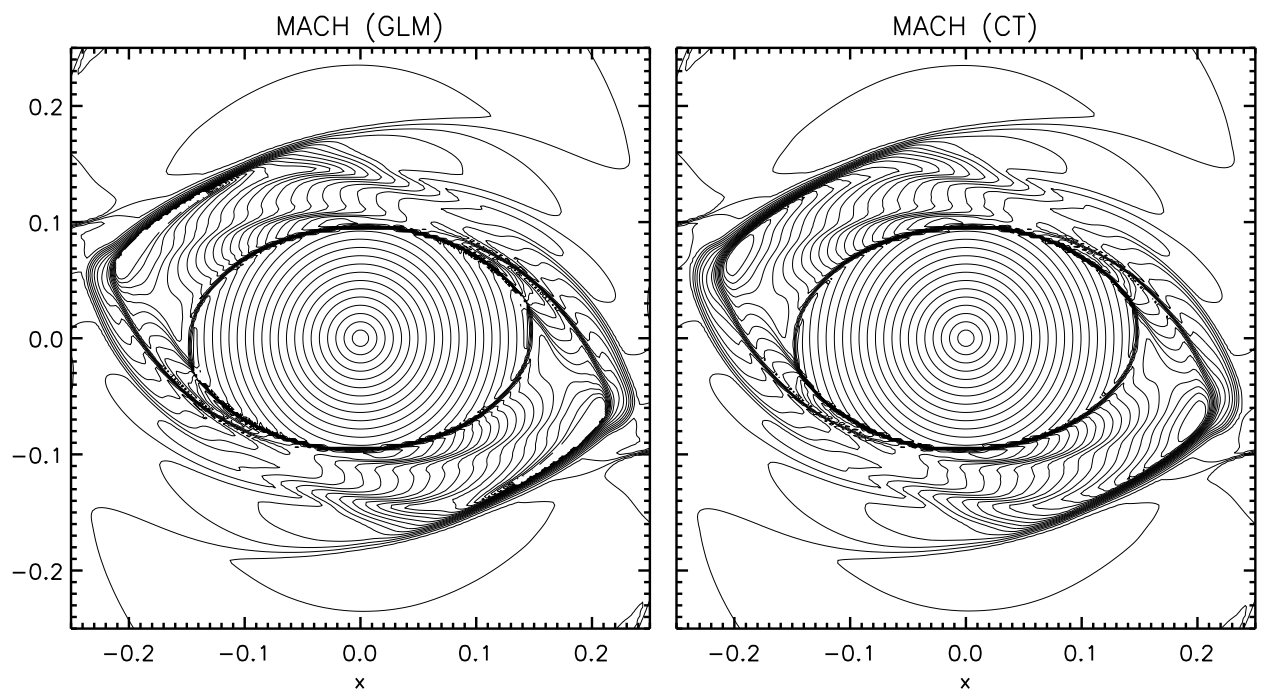


Figure 13: A zoom in the central region of the rotor problem at time  $t = 0.15$ , showing 20 levels ( $0 \leq M \leq 4$ ) of contour profiles of the sonic Mach number. Results for the GLM and CT schemes are shown on the left and right panels, respectively.

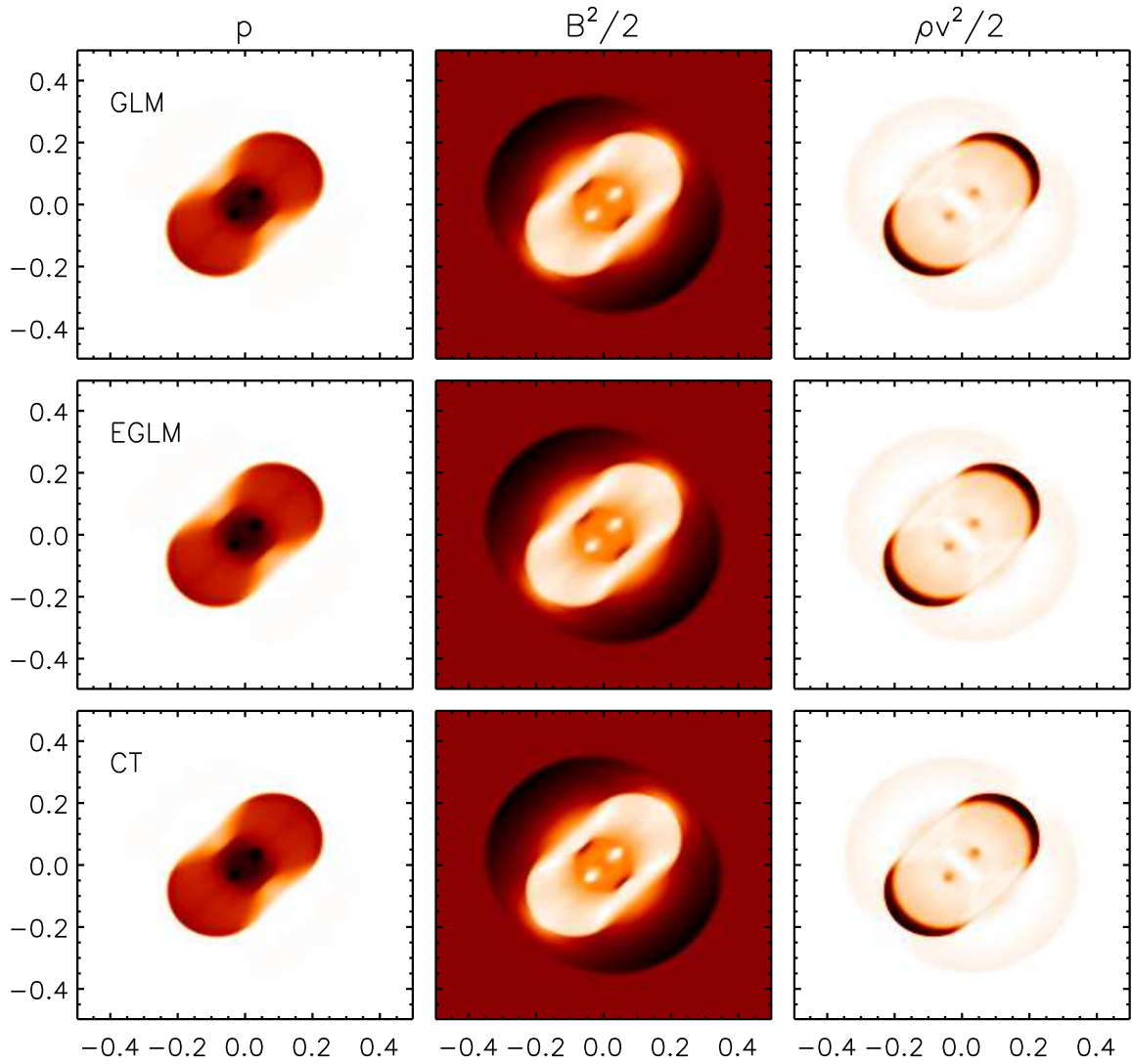


Figure 14: Two dimensional cuts in the  $xz$  plane of gas pressure, magnetic and kinetic energy densities for the GLM (top), EGLM (middle) and CT (bottom) schemes, at  $t = 0.02$  for the first blast wave problem. Pressure values range from 1.0 (white) to 42.4 (black). The magnetic energy ranges from 25.2 (white) to 64.9 (black) while the kinetic energy density spans from 0.0 (white) to 33.1 (black).

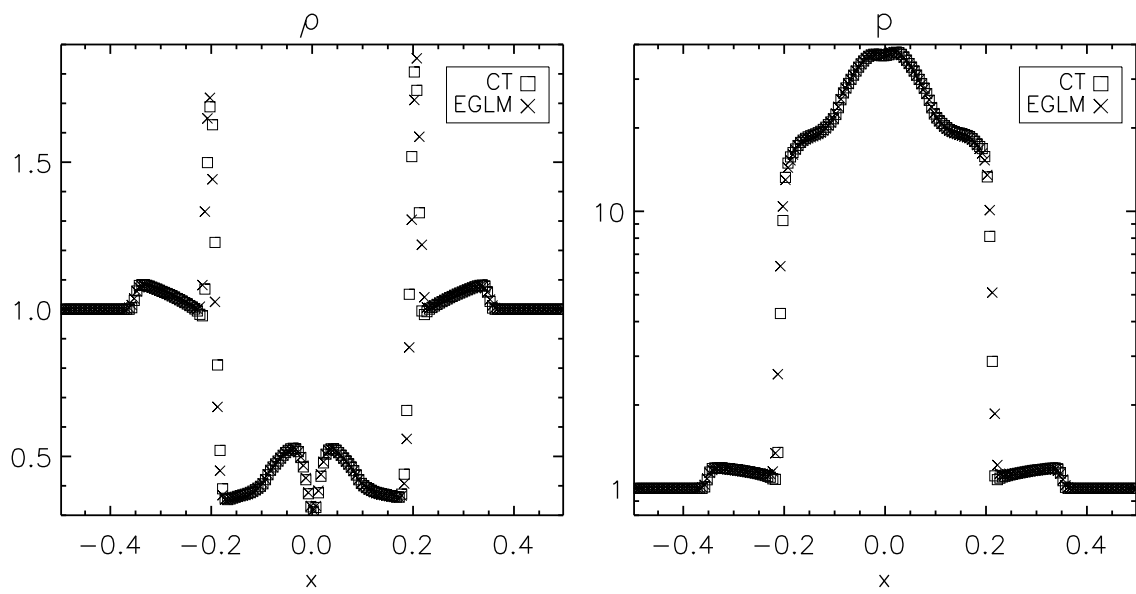


Figure 15: Density and pressure profiles, the latter on logarithmic scale, along  $x$  at  $y, z = 0$ , at time  $t = 0.02$ . Results obtained with the CT and EGLM schemes are shown using box and cross symbols, respectively.

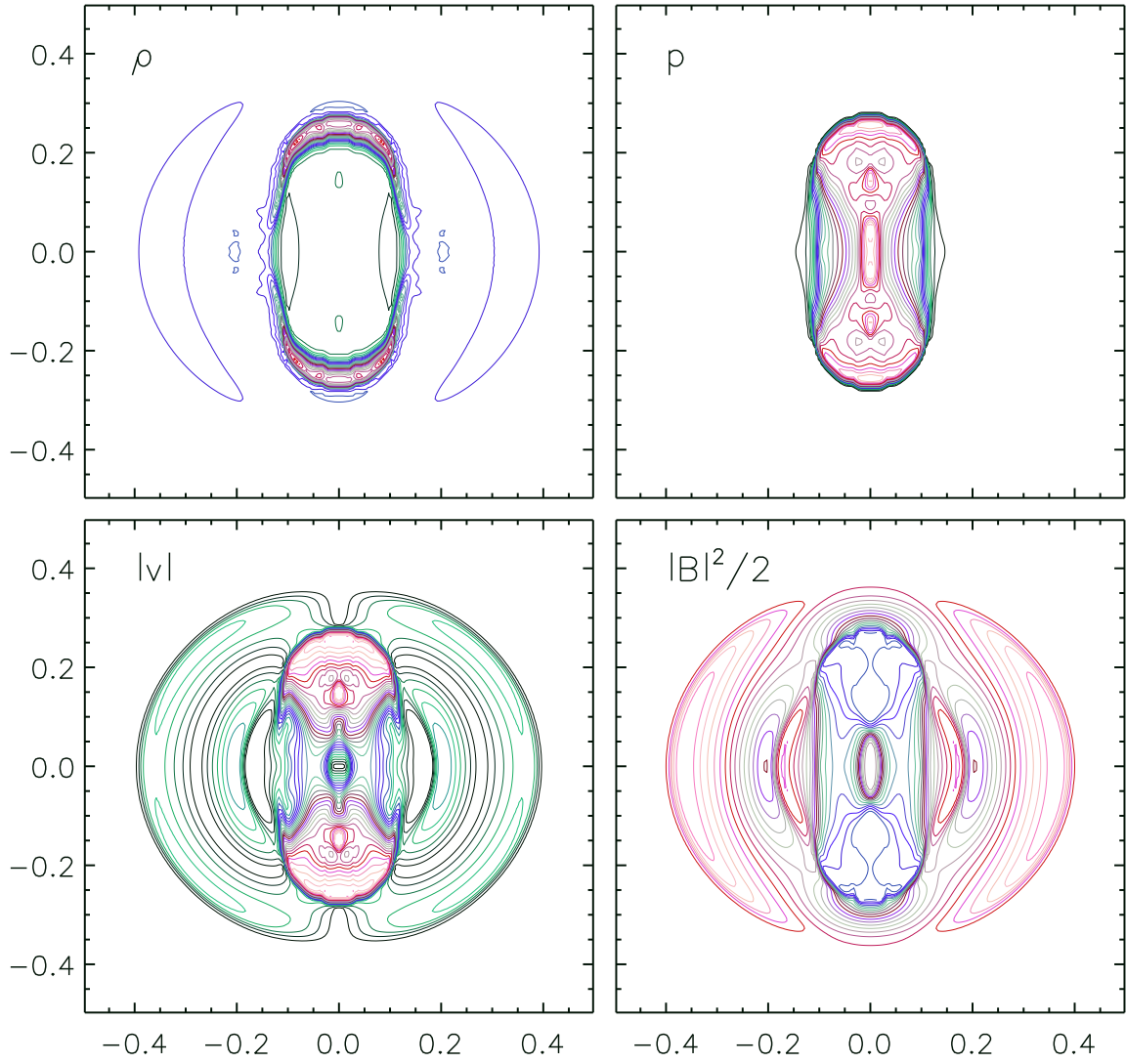


Figure 16: Density, pressure, velocity and magnetic energy contours (30 levels) for the CTU-EGLM scheme at  $t = 2.5 \cdot 10^{-3}$  in the  $xz$  plane. Density values range from 0.18 to 3.2 while pressure spans from 0.9 to 2290. The absolute value of velocity ranges from 0.0 to 47 while the magnetic energy spans from 2817 to 5932.